Conformational Flexibility and Strand Arrangements of the Membrane-Associated HIV Fusion Peptide Trimer Probed by Solid-State NMR Spectroscopy†

Zhaoxiong Zheng,‡ Rong Yang,§ Michele L. Bodner,‡ and David P. Weliky*,‡

Department of Chemistry, Michigan State University, East Lansing, Michigan 48824, and Department of Physiology and Cellular Biophysics, Columbia University, New York, New York 11032

Received August 5, 2006; Revised Manuscript Received August 30, 2006

ABSTRACT: The human immunodeficiency virus (HIV) fusion peptide (HFP) is the N-terminal apolar region of the HIV gp41 fusion protein and interacts with target cell membranes and promotes membrane fusion. The free peptide catalyzes vesicle fusion at least to the lipid mixing stage and serves as a useful model fusion system. For gp41 constructs which lack the HFP, high-resolution structures show trimeric protein and suggest that at least three HFPs interact with the membrane with their C-termini in close proximity. In addition, previous studies have demonstrated that HFPs which are cross-linked at their C-termini to form trimers (HFPtr) catalyze fusion at a rate which is 15−40 times greater than that of non-cross-linked HFP. In the present study, the structure of membrane-associated HFPtr was probed with solid-state nuclear magnetic resonance (NMR) methods. Chemical shift and intramolecular $^{13}CO-^{15}N$ distance measurements show that the conformation of the Leu-7 to Phe-11 region of HFPtr has predominant helical conformation in membranes without cholesterol and β strand conformation in membranes containing ∼30 mol % cholesterol. Interstrand $^{13}CO-^{13}CO$ and $^{13}CO-^{15}N$ distance measurements were not consistent with an in-register parallel strand arrangement but were consistent with either (1) parallel arrangement with adjacent strands two residues out-of-register or (2) antiparallel arrangement with adjacent strand crossing between Phe-8 and Leu-9. Arrangement 1 could support the rapid fusion rate of HFPtr because of placement of the apolar N-terminal regions of all strands on the same side of the oligomer while arrangement 2 could support the assembly of multiple fusion protein trimers.

Enveloped viruses such as human immunodeficiency virus (HIV[1]) are surrounded by a membrane and infect cells through fusion between the viral membrane and the target cell membrane (*1*, *2*). This process is mediated by envelope proteins which traverse the viral membrane (*3*). For HIV, the gp41 envelope protein has a ∼170-residue ectodomain region which lies outside the viral membrane and contains a N-terminal ∼20-residue apolar "fusion peptide" (HFP). The HFP interacts with the target cell membrane and plays an essential role in membrane fusion (*4*). Peptides composed of the HFP sequence induce fusion between large unilamellar vesicles (LUVs) and between erythrocytes (*5*, *6*). There are similar mutation/fusion activity relationships for HFP-induced fusion and HIV-induced fusion, which suggests that HFP is a useful model system to understand some aspects of viral/target cell fusion (*7*−*10*). There is also evidence for participation of other regions of gp41 in membrane fusion (*11*−*14*). There are atomic-resolution structures of the "soluble ectodomain" of gp41 which does not contain the ∼30 N-terminal residues of gp41 (including the HFP) (*2*, *15*−*19*). These structures are believed to correspond to the conformation after fusion has occurred and perhaps during some fusion steps (*20*). The gp41 molecules form a trimer in the soluble ectodomain structure with the three N-termini in close proximity at the end of an in-register helical coiled-coil. It has therefore been hypothesized that during viral/target cell fusion, at least three HFPs insert into the target cell membrane with their C-termini in close proximity. There is some antibody-based evidence for this hypothesis (*21*).

† This work was supported by NIH award AI47153 to D.P.W.

* Corresponding author. Tel: 517-355-9715. Fax: 517-353-1793. E-mail: weliky@chemistry.msu.edu.

‡ Michigan State University.

§ Columbia University.

[1] Abbreviations: CD, circular dichroism; *CP*, cross-polarization; CSA, chemical shift anisotropy; d_{CC}, $^{13}C-^{13}C$ dipolar coupling; d_{CN}, $^{13}C-^{15}N$ dipolar coupling; DCM, dichloromethane; D-GFF, doubly labeled GFF; D-NAL, 1-^{13}C, N-^{13}C doubly labeled NAL; DTPC, 1,2-di-*O*-tetradecyl-*sn*-glycero-3-phosphocholine; DTPG, 1,2-di-*O*-tetradecyl-*sn*-glycero-3-phospho-*rac*-(1-glycerol) sodium salt; DPhPE, 1,2-di-*O*-phytanyl-*sn*-glycero-3-phosphoethanolamine; ESR, electron spin resonance; FMOC, 9-fluorenylmethoxycarbonyl; fpCTDQBU, constant-time double-quantum buildup with finite pulses; fpRFDR-CT, constant-time finite-pulse rf-driven recoupling; GFF, glycyl-L-phenylalanyl-L-phenylalanine; HEPES, *N*-(2-hydroxyethyl)piperazine-*N*′-2-ethanesulfonic acid; HIV, human immunodeficiency virus; HFP, HIV fusion peptide; HFPdm, HIV fusion peptide dimer; HFPmn, HIV fusion peptide monomer; HFPtr, HIV fusion peptide trimer; HPLC, high-performance liquid chromatography; IR, infrared; LM3, lipid mixture 3; LM3e, ether-linked lipid mixture 3; LUV, large unilamellar vesicle; MAS, magic angle spinning; NAL, N-acetyl-L-leucine; NMP, *N*-methylpyrrolidone; NMR, nuclear magnetic resonance; PC-PG, 4:1 POPC:POPG mixture, PDB, Protein Data Bank; PI, phosphatidylinositol; POPC, 1-palmitoyl-2-oleoyl-*sn*-glycero-3-phosphocholine; POPE, 1-palmitoyl-2-oleoyl-*sn*-glycero-3-phosphoethanolamine; POPG, 1-palmitoyl-2-oleoyl-*sn*-glycero-3-phospho-*rac*-(1-glycerol); POPS, 1-palmitoyl-2-oleoyl-*sn*-glycero-3-phospho-L-serine; rf, radio frequency; r_{CC}, $^{13}C-^{13}C$ distance; r_{CN}, $^{13}C-^{15}N$ distance; REDOR, rotational-echo double resonance; RFDR, radio frequency-driven recoupling; SIMPSON, simulation program for solid-state NMR spectroscopy; TBME, *tert*-butyl methyl ether; TFA, trifluoroacetic acid; TPPM, two-pulse phase-modulation; 2D, two-dimensional.

10.1021/bi0615902 CCC: $33.50
Published on Web 10/10/2006

A variety of experimental methods have shown that membrane-associated HFP can assume either helical or nonhelical structure (*5*, *7*, *22*−*32*). Models for the helical structure have been developed based on nuclear magnetic resonance (NMR), electron spin resonance (ESR), infrared (IR), and circular dichroism (CD) data, as well as computer simulations (*33*−*39*). A β hairpin model for nonhelical structure has been proposed based on IR and surface activity measurements in membranes (*40*).

Fluorescence, ESR, IR, and solid-state NMR data also suggest that the nonhelical HFPs in membranes form oligomeric structures (*10*, *41*−*44*). These oligomeric structures may be important as evidenced by envelope protein trimerization and by experiments and modeling which indicate that the fusion site contains multiple trimers and a corresponding high HFP concentration (*17*, *18*, *45*). Additionally, the V2E mutation in gp41 dominantly interferes with HIV fusion and infectivity and suggests that oligomeric HFP is important in viral/target cell fusion (*8*, *10*).

In an effort to mimic the oligomeric HFP topology suggested by the gp41 soluble ectodomain structures, HFP oligomers in dimeric (HFPdm) and trimeric form (HFPtr) have been synthesized with chemical cross-linking at their peptide C-termini. Cross-linking was accomplished with either cysteine or lysine residues. Comparative measurements were made between HFPdm and HFPtr and monomeric HFP (HFPmn) (*28*, *46*). All three constructs contained additional C-terminal lysines to inhibit intermolecular self-association in aqueous solution, and buffer conditions were found with minimal self-association. The rate of peptide-induced intervesicle lipid mixing was 15−40 times higher for HFPtr relative to HFPmn and suggests that oligomeric HFP topology plays a significant role in membrane fusion. The HFPdm rate was intermediate between the rates of HFPmn and HFPtr. Enhanced fusogenicity has also been observed for other oligomeric constructs which contain fusion peptides and support the hypothesis that oligomeric fusion peptide topology is one factor which contributes to fusion (*47*−*49*).

Solid-state NMR structural experiments have been carried out on membrane-associated HFPmn, HFPdm, and HFPtr. Backbone ^{13}C carbonyl chemical shift and 2D exchange measurements suggest a predominant β strand conformation for HFPmn associated with membranes whose lipid headgroup and cholesterol composition is comparable to that found in host cells of the virus (*25*). In addition, the Phe-8 carbonyl chemical shift of HFPdm and HFPtr in the same host cell-like membrane composition is upfield of the random coil value and is more consistent with β strand conformation than with helical conformation (*28*, *46*). For HFPtr associated with membranes which do not contain cholesterol, the Phe-8 chemical shift is downfield of the random coil value and is more consistent with helical conformation. In the present study, membrane-associated HFPtr was investigated using solid-state NMR methods including ^{13}C chemical shifts and $^{13}C-^{15}N$ distance measurements to probe local peptide conformation and $^{13}C-^{13}C$ and $^{13}C-^{15}N$ distance measurements to probe interpeptide β strand arrangement. It had previously been proposed that the increased lipid mixing rate induced by β strand HFPdm and HFPtr was related to predominant parallel strand arrangement enforced by the C-terminal cross-linking (*28*). For this arrangement, the apolar N-terminal regions of the three strands would be on the same side of the oligomer and the resulting large apolar volume would cause significant membrane perturbation and rapid fusion rate. This structure would differ from the mixture of parallel and antiparallel arrangements observed for membrane-associated HFPmn (*43*). In this paper, an in-register parallel strand model for HFPtr was tested using a solid-state NMR $^{13}CO-^{13}CO$ distance measurement approach which had been previously applied to probe structure in β amyloid fibrils (*50*, *51*).

The $^{13}C-^{15}N$ distances were determined with the rotational-echo double-resonance (REDOR) technique which is an approach to measure heteronuclear dipolar couplings under magic angle spinning (MAS) (*52*−*60*). MAS reduces solid-state NMR linewidths and increases signal-to-noise, and the dipolar coupling d_{CN} depends on r_{CN} distance as $(r_{CN})^{-3}$. The $^{13}C-^{13}C$ distances were determined with a constant-time double-quantum buildup with finite pulses (fpCTDQBU) technique which is an approach to measure homonuclear dipolar couplings under MAS (*51*, *61*−*65*). The dipolar coupling d_{CC} depends on r_{CC} distance as $(r_{CC})^{-3}$. This fpCTDQBU method is a finite pulse variant of the CTDQBU technique developed by Bennett et al., and incorporation of finite pulses increases the signal-to-noise, as will be discussed in the Results section (*64*). The utility of finite pulses was first demonstrated by Ishii in the related constant-time finite-pulse radiofrequency-driven recoupling (fpRFDR-CT) method, and the two techniques are robust methods for determination of d_{CC} with weak dependences on chemical shift differences, chemical shift anisotropy (CSA), resonance offset, spin relaxation, and rf inhomogeneity (*51*, *65*).

Quantitative analysis of the REDOR and fpCTDQBU data requires explicit computer simulation of the experiments as a function of molecular geometry parameters. The SIMPSON computer program was used for this purpose and allows input of the geometric parameters as well as the NMR parameters used in the experiment (*66*). The HFPtr results in the present paper also rely on careful calibration of the REDOR and fpCTDQBU experiments with model compounds for which the $^{13}C-^{15}N$ and $^{13}C-^{13}C$ distances are known and comparable to distances in HFPtr structural models.

MATERIALS AND METHODS

Materials. Rink amide resin and Wang Resin were purchased from Advanced Chemtech (Louisville, KY). *N*-α-Fluorenylmethoxycarbonyl (FMOC)-*N*′-ϵ-4-methyltrityl-L-lysine (FMOC-Lys(Mtt)) was purchased from Calbiochem-Novabiochem (La Jolla, CA), and FMOC amino acids and FMOC-β-Ala-Wang resin were obtained from Peptides International (Louisville, KY). For the labeled peptide syntheses, labeled amino acids were purchased from Icon Services Inc (Summit, NJ) and were FMOC-protected using literature methods (*67*, *68*). In addition, FMOC-1-^{13}C glycine was purchased from Sigma-Aldrich (St. Louis, MO). 1-Palmitoyl-2-oleoyl-*sn*-glycero-3-phosphocholine (POPC), 1-palmitoyl-2-oleoyl-*sn*-glycero-3-phospho-*rac*-(1-glycerol) (POPG), 1-palmitoyl-2-oleoyl-*sn*-glycero-3-phosphoethanolamine (POPE), 1-palmitoyl-2-oleoyl-*sn*-glycero-3-phospho-L-serine (POPS), phosphatidylinositol (PI), sphingomyelin, 1,2-di-*O*-tetradecyl-*sn*-glycero-3-phosphocholine (DTPC), 1,2-di-*O*-tetradecyl-*sn*-glycero-3-phospho-*rac*-(1-glycerol) sodium salt (DTPG), and 1,2-di-*O*-phytanyl-*sn*-glycero-3-phosphoethanolamine

(DPhPE) were purchased from Avanti Polar Lipids (Alabaster, AL). *N*-(2-Hydroxyethyl)piperazine-*N*-2-ethanesulfonic acid (HEPES) was obtained from Sigma-Aldrich (St. Louis, MO). The buffer solution used in the study contained 5 mM HEPES (pH 7.0) with 0.01% NaN_3.

HFPtr Synthesis. The "HFPtr-$L7_CF11_N$" fusion peptide trimer was synthesized with sequence $(AVGIGALFLGFL-GAAGSTMGARSWKKKKKK)_3$-$A_\beta$ and with a ^{13}CO label at Leu-7 and a ^{15}N label at Phe-11 on each strand. The related "HFPtr-$F8_CL9_N$" trimer was synthesized with sequence $(AVGIGALFLGFLGAAGSTWMGARSKKKKKK)_3$-$A_\beta$ and with a ^{13}CO label at Phe-8 and a ^{15}N label at Leu-9 on each strand. Residues in the N-termini of HFPtr correspond to the 23 N-terminal residues (sequence AVGIGALFLGFL-GAAGSTMGARS) of the LAV_{1a} strain of the HIV-1 gp41 envelope fusion protein. HFPtr synthesis began with coupling of FMOC-Lys(Mtt) and activated β-Ala-Wang resin (*46*). A lysine trimer backbone was then formed with coupling of FMOC-Lys(Mtt) followed by coupling with *N*-α-FMOC-*N*′-ϵ-*tert*-butoxycarbonyl-L-lysine (FMOC-Lys(Boc)). Prior to the second and third couplings, the Mtt group on the lysine side chain was removed with 1% trifluoroacetic acid (TFA) in dichloromethane (DCM). The rest of the trimer was then synthesized using a peptide synthesizer (ABI 431A, Foster City, CA) equipped for standard FMOC chemistry. Cleavage of HFPtr from the resin was done in a 3 h reaction with a mixture of TFA−H_2O−phenol−thioanisole−ethanedithiol in a 33:2:2:2:1 volume ratio, and purification was done with reversed-phase HPLC and a preparative C_{18} column (Vydac, Hesperia, CA) and a water−acetonitrile gradient containing 0.1% TFA. Mass spectroscopy was used for peptide identification.

N-Acetyl-L-leucine (NAL). 1-^{13}C, N-^{13}C doubly labeled NAL (D-NAL) was synthesized as a setup compound for fpCTDQBU experiments (*69*). Synthesis of D-NAL began with addition of 1-^{13}C, ^{15}N leucine to glacial acetic acid and heating to 100 °C. 1-^{13}C acetic anhydride was then added, the solution was cooled to 80 °C, and water was added to react with any excess acetic anhydride. The D-NAL product was washed with cyclohexane, and the cyclohexane was subsequently removed under vacuum. Residual solvents were removed by water aspirator vacuum, drying in a vacuum desiccator, and dissolution in water followed by lyophilization. Solution ^1H and ^{13}C NMR confirmed the identity, purity, and labeling of D-NAL. The NAL sample for solid-state NMR was prepared by aqueous dissolution of a 1:9 mixture of D-NAL and unlabeled NAL (ICN, Aurora, OH) followed by slow evaporation of the water. The polycrystalline solid was ground with a mortar and pestle. The intramolecular $^{13}C-^{13}C$ distance of D-NAL in the crystal is 3.1 Å (*70*).

Glycyl-L-phenylalanyl-L-phenylalanine (GFF). Doubly labeled GFF (D-GFF) was synthesized with ^{13}CO labels at Gly-1 and Phe-3 and was a model compound for the fpCTDQBU experiments. D-GFF synthesis began with dissolution of FMOC-1-^{13}C-Phe in a *N*-methylpyrrolidone (NMP)/DCM mixture followed by 2 h coupling of the amino acid to unsubstituted Wang resin using a mixture of 1.0 M *N*,*N*′-dicyclohexylcarbodiimide in NMP and 0.1 M 4-dimethylaminopyridine in dimethylformamide. Unreacted amino groups on the resin were benzoylated with benzoic anhydride. Standard FMOC chemistry was used for the remaining synthesis with 4 and 8 h coupling times for FMOC-Phe and FMOC-1-^{13}C-Gly, respectively. D-GFF was cleaved from the resin in a 3 h reaction with a mixture of TFA−water−phenol in a 33:2:2 volume ratio and precipitated by addition of *tert*-butyl methyl ether (TBME). The yellowish-white precipitate was washed with TBME, centrifuged, lyophilized, dissolved in water, and passed through a 4−8 μm filter. After slow evaporation of the water, colorless and needle-like D-GFF hemihydrate crystals were harvested. A small aliquot of the crystals was dissolved in dimethylsulfoxide-d_6, and subsequent ^1H and ^{13}C NMR spectroscopy confirmed the purity and labeling of D-GFF. The solid-state NMR sample of GFF was prepared by aqueous dissolution of D-GFF and unlabeled GFF (Sigma-Aldrich) in a 1:49 ratio followed by slow evaporation of solvent. The polycrystalline solid was ground with a mortar and pestle. The intramolecular $^{13}C-^{13}C$ distance of D-GFF in the crystal is 5.40 Å (*71*).

I4 Peptide. A 17-residue acetylated and amidated "*I4*" peptide with sequence Ac-AEAAAKEAAAKEAAAKA-NH_2 was synthesized with a ^{13}CO label at Ala-9 and a ^{15}N label at Ala-13. The solid-state NMR *I4* peptide sample was lyophilized from aqueous solution and is predominantly (83 ± 6%) α helical at Ala-9 (*72*). The two labeled nuclei should have a $^{13}C-^{15}N$ internuclear distance of ∼4.1 Å in the helical structure.

Lipid Preparation. HFPtr samples were prepared using three lipid/cholesterol mixtures: (a) "PC-PG" had POPC and POPG in a 4:1 mol ratio and has a headgroup composition similar to that used in previous fusion peptide and fusion protein biophysical studies (*73*−*76*); (b) "LM3" had POPC, POPE, POPS, sphingomyelin, PI, and cholesterol in a 10:5:2:2:1:10 mol ratio and reflects the lipid headgroup and cholesterol composition of cells infected by HIV (*77*, *78*); and (c) "LM3e" had DTPC, DTPG, DPhPE, and cholesterol in a 9:3:3:10 mol ratio and was similar to LM3 in lipid headgroup and cholesterol composition but contained ether-linked rather than ester-linked lipids to eliminate natural abundance lipid ^{13}CO signals. Lipid and cholesterol powders were dissolved in chloroform. The chloroform was removed under a stream of nitrogen followed by overnight vacuum pumping. Lipid dispersions were formed by addition of 5 mM pH 7.0 HEPES buffer followed by homogenization with 10 freeze−thaw cycles. Large unilamellar vesicles (LUVs) were prepared by extrusion through a filter with 100 nm diameter pores (*79*).

Solid-State NMR Sample Preparation. The samples were made in a manner similar to that used for doing functional fusion assays (*46*). HFPtr (0.1−0.2 μmol as determined by A_{280}) was dissolved in ∼2 mL of 5 mM HEPES buffer, and LUVs (∼30 μmol total lipid) were prepared in ∼2 mL of buffer. The peptide and LUV solutions were mixed and kept at room temperature overnight followed by ultracentrifugation at 35 000 rpm for 5 h at 4 °C. The peptide/lipid pellet formed after ultracentrifugation was transferred by spatula to a 4 mm diameter MAS NMR rotor. Unbound HFPtr is predominantly monomeric under these conditions and does not pellet. For the HFPtr and other samples, the rotor volume of ∼40 μL was filled.

Solid-State NMR Spectroscopy. Experiments were done on a 9.4 T spectrometer (Varian Infinity Plus, Palo Alto, CA) using a MAS probe in double resonance $^{13}C/^1H$ configuration for fpCTDQBU experiments and in triple resonance $^{13}C/^1H/^{15}N$ configuration for REDOR experiments.

Relative to the triple resonance configuration, the double resonance configuration has 1.5 times higher ^{13}C sensitivity. The NMR detection channel was tuned to ^{13}C at 100.8 MHz, the decoupling channel was tuned to ^{1}H at 400.8 MHz, and for REDOR the third channel was tuned to ^{15}N at 40.6 MHz. ^{13}C shifts were externally referenced to the methylene resonance of adamantane at 40.5 ppm, which allowed direct comparison with ^{13}C shifts of proteins in aqueous solution (*80*, *81*). ^{15}N shifts were referenced to $(^{15}NH_4)_2SO_4$ at 20 ppm. Experiments used a MAS frequency of 8000 ± 2 Hz, and spacers were used to restrict samples to the central 2/3 rotor volume (~40 μL) in which rf field variation was less than 10%.

Experiments were performed at −50 °C rather than room temperature in order to achieve more efficient cross-polarization (*CP*) and greater signal per ^{13}C nucleus. There are similar ^{13}C backbone chemical shifts at both low temperature and room temperature, suggesting that cooling the sample does not cause significant peptide structural changes (*29*). The ^{1}H, ^{13}C, and ^{15}N pulse lengths and the *CP* matching condition were approximately obtained by running direct pulse and *CP* experiments on adamantane and $(^{15}NH_4)_2SO_4$. Further parameter optimization was made with model compounds. Recycle delays were between 1 and 2 s.

REDOR Spectroscopy. The "all-but-one ^{15}N π pulse" version was used to suppress natural abundance ^{13}C signals and selectively detect the labeled Phe-8 ^{13}CO signal of HFPtr-$F8_CL9_N$ (*27*, *52*). An initial 2 ms *CP* was done with a ramped 40−50 kHz ^{13}C rf field and a ~60 kHz ^{1}H rf field and was followed by a 1 ms dephasing period and then ^{13}C detection. A single ~50 kHz ^{13}C refocusing π pulse was placed at the midpoint of the dephasing period, and two-pulse phase-modulation (TPPM) ^{1}H decoupling of ~90 kHz was applied during dephasing and detection (*82*). The ^{13}C transmitter was set to ~155 ppm, and the ^{15}N transmitter was set to ~115 ppm. An "S_0" and an "S_1" acquisition were obtained. The dephasing period during the S_1 acquisition contained a 40 kHz ^{15}N π pulse at the midpoint and at the end of each rotor cycle except for the fourth and the eighth cycles. XY-8 phase cycling (0, 90, 0, 90, 90, 0, 90, 0) was used for the ^{15}N pulses (*83*). The ^{15}N pulses disrupted averaging of the $^{13}C-^{15}N$ dipolar coupling by MAS and led to selective attenuation of the Phe-8 ^{13}CO signal. The S_0 acquisition did not contain ^{15}N pulses, and $^{13}C-^{15}N$ dipolar coupling was efficiently averaged by MAS and did not lead to ^{13}C signal attenuation. The selective spectrum of Phe-8 ^{13}CO was obtained by subtracting the S_1 signal from the S_0 signal.

$^{13}CO-^{15}N$ distances were measured with an "alternating $^{15}N/^{13}C$ π pulse" version of REDOR (*53*, *84*). For the S_1 acquisition, the dephasing period of length τ_i included a ~40 kHz ^{15}N π pulse at the midpoint of each rotor cycle and a ~50 kHz ^{13}C π pulse at the end of each rotor cycle except for the last cycle. The S_0 acquisition did not include ^{15}N π pulses during the dephasing period. TPPM ^{1}H decoupling of ~90 kHz was applied during dephasing and detection. ^{13}C signals were attenuated by $^{13}C-^{15}N$ dipolar coupling in the S_1 acquisition but not in the S_0 acquisition. Spectra were acquired for different τ_i, and the difference between the ^{13}CO S_0 and S_1 signal intensities divided by the S_0 signal intensity $(\Delta S/S_0)_i$ was the experimental parameter used to determine $^{13}CO-^{15}N$ dipolar couplings and distances. XY-8 phase cycling was used for the ^{15}N π pulses and for all of the ^{13}C π pulses except the final pulse. Individual S_0 or S_1 transients were added with phase cycling: ^{1}H $\pi/2$, 0, 180, 0, 180; ^{1}H CP, 90, 90, 90, 90; ^{13}C CP 270, 270, 180, 180; final ^{13}C π pulse, 270, 270, 180, 180; receiver, 180, 0, 90, 270.

The S_0 signal intensity of the *I*4 peptide was used to optimize ^{1}H $\pi/2$, ^{1}H decoupling, ^{13}C π, and *CP* rf fields, and the $\Delta S/S_0$ values of the *I*4 peptide were used to optimize the ^{15}N π rf field.

fpCTDQBU Spectroscopy. The NMR sequence has the form $CP_{90\pm\zeta}-(fpRFDR)_L-\pi/2_\zeta-\pi/2_0-(fpRFDR)_M-\pi/2_{180}-\pi/2_{90}-(fpRFDR)_N-acquisition$ where *L*, *M*, and *N* refer to the number of rotor cycles in each *fpRFDR* period and the other subscripts refer to the rf phases (*64*). Generation of transverse ^{13}C magnetization during *CP* was followed by *fpRFDR* periods which contained finite ^{13}C π pulses and during which the magnetization may be reduced by net $^{13}C-^{13}C$ dipolar coupling. The transverse magnetization was then detected during the acquisition period. For each value of ζ = 0, 90, 180, and 270, a distinct spectrum was obtained. The $\pi/2_{180}-\pi/2_{90}$ pulse pair served to refocus $^{13}C-^{13}C$ dipolar coupling so that there was no net coupling over the period which began *N* rotor cycles prior to the pulse pair and ended at the beginning of acquisition. For ζ = 90 or 270, there was similarly no net dipolar coupling over the period which began after *CP* and ended *L* rotor cycles after the $\pi/2_\zeta-\pi/2_0$ pulse pair. By contrast, for ζ = 0 or 180, there was net dipolar coupling during the dephasing period of duration $\tau_i = 2L \times \tau_R$ where τ_R is the rotor period. For each value of τ_i, S_0 and S_1 signals were acquired with $S_0 = S_{\zeta=90} + S_{\zeta=270}$ and $S_1 = S_{\zeta=0} + S_{\zeta=180}$. The parameter $(\Delta S/S_0)_i$ was calculated as in the REDOR experiment and served as the experimental constraint for determination of $^{13}C-^{13}C$ dipolar couplings and distances.

A single value of *M* and a single value of $L + M + N$ were used for all τ_i values in a given experiment. The transverse magnetization therefore evolved for a single "constant-time" for all τ_i, and the contribution to $(\Delta S/S_0)_i$ from effects other than the $^{13}C-^{13}C$ dipolar couplings was approximately independent of τ_i (*85*). Experiments were initially attempted with the non-constant-time and higher signal-to-noise sequence $CP_{90\pm\zeta}-(fpRFDR)_L-\pi/2_\zeta-/2_0-(fpRFDR)_L-acquisition$, but the $(\Delta S/S_0)_i$ values obtained with this sequence for model compounds fitted poorly to simulations based on known $^{13}CO-^{13}CO$ distances. Constant-time was critical for quantitative interpretation of the data.

Other experimental details included the following: (*1*) the ^{13}C transmitter was set to ~177 ppm; (*2*) the *CP* period had 2 ms duration, ramped 40−50 kHz ^{13}C rf field, and a ~54 kHz ^{1}H rf field; (*3*) ^{13}C $\pi/2$ pulses had ~43 kHz rf field; (*4*) *fpRFDR* periods had one ^{13}C π pulse every two rotor cycles, and the pulse was centered in the two cycle increment; and (*5*) continuous-wave ^{1}H decoupling at ~95 kHz and ~60 kHz was applied during the *fpRFDR* and *acquisition* periods, respectively. XY-8 phase cycling was used for the *fpRFDR* π pulse train, and the other pulses had the following phases: ^{1}H $\pi/2$, 180, 0, 0, 180; ^{1}H *CP*, 90, 90, 90, 90; ^{13}C *CP* 270, 180, 270, 180. The corresponding values of ζ were 0, 90, 180, 270. Calibration of rf fields was done using the D-NAL sample. Both the D-NAL and D-GFF samples were used to study the effects of "finite" ^{13}C π pulses, i.e., pulses with longer duration and concomitant smaller rf field.

Experimental Data Analysis. Integration of signal intensities in the isotropic carbonyl regions of the S_0 and S_1 spectra for a particular dephasing time τ_i yielded values denoted as S_{0i} and S_{1i}. $(\Delta S/S_0)_i^{\exp}$ is a normalized dephasing parameter:

$$\left(\frac{\Delta S}{S_0}\right)_i^{\exp} = \frac{S_{0i} - S_{1i}}{S_{0i}} = 1 - \frac{S_{1i}}{S_{0i}} \quad (1)$$

For each pair of S_{0i}, S_{1i} spectra, an experimental uncertainty σ was calculated as the root mean squared deviation of integrated intensities in 24 regions of the spectra without signal. The uncertainty in $(\Delta S/S_0)_i^{\exp}$ is denoted $\sigma_i^{\exp}$ and was calculated (*86*)

$$\sigma_i^{\exp} = \frac{\sigma}{S_{0i}}\sqrt{1 + \frac{S_{1i}^2}{S_{0i}^2}} = \frac{\sigma S_{1i}}{S_{0i}}\sqrt{\frac{1}{S_{1i}^2} + \frac{1}{S_{0i}^2}} \quad (2)$$

Determination of distances between labeled nuclei relies on comparison of $(\Delta S/S_0)_i^{\exp}$ and $(\Delta S/S_0)_i^{\mathrm{sim}}$ where sim $\equiv$ simulated. The $(\Delta S/S_0)_i^{\mathrm{sim}}$ only consider the labeled spins whereas $(\Delta S/S_0)_i^{\exp}$ has contributions from natural abundance nuclei and other effects. The $(\Delta S/S_0)_i^{\exp}$ values were therefore adjusted to remove these other contributions, and the resulting corrected $(\Delta S/S_0)_i^{\mathrm{cor}}$ values were compared to $(\Delta S/S_0)_i^{\mathrm{sim}}$ to obtain distances between labeled nuclei. We briefly discuss determination of $(\Delta S/S_0)_i^{\mathrm{cor}}$ for the REDOR measurements on the HFPtr-L7$_C$F11$_N$ samples. The Supporting Information section provides a detailed description of the derivation of $(\Delta S/S_0)_i^{\mathrm{cor}}$ for all of the samples and experiments.

Determination of $(\Delta S/S_0)_i^{\mathrm{cor}}$ relies on consideration of contributions to S_0 and S_1 from ^{13}CO nuclei in different environments. The following parameters/approximations are used for REDOR of HFPtr-L7$_C$F11$_N$: (1) There is 99% labeling of the Leu-7 ^{13}CO and Phe-11 ^{15}N sites. $S_1 = S_0$ for a labeled Leu-7 ^{13}CO in a peptide strand with a Phe-11 ^{14}N. (2) $S_1 = 0$ for a labeled Leu-7 ^{13}CO separated by one or two bonds from a natural abundance ^{15}N at Phe-8 or Leu-7. The Leu-7 S_1 is not affected by other natural abundance ^{15}N. (3) $S_1 = 0$ for natural abundance backbone ^{13}COs at Gly-10 or Phe-11 which are separated by one or two bonds from the labeled Phe-11 ^{15}N. $S_1 = S_0$ for other natural abundance backbone ^{13}CO sites. Criteria (1) and (2) are based on the close distance ($\leq$2.5 Å) and consequent strong ($\geq$200 Hz) dipolar coupling of ^{13}CO and ^{15}N nuclei separated by one or two bonds.

As described in the Supporting Information, an expression for $(\Delta S/S_0)_i^{\mathrm{cor}}$ can be derived:

$$\left(\frac{\Delta S}{S_0}\right)_i^{\mathrm{cor}} = \frac{1 - U_C + nA_C}{(1 - U_C - U_N - 2B_N)}\left(\frac{\Delta S}{S_0}\right)_i^{\exp} - \frac{2A_C + 2A_N}{(1 - U_C - U_N - 2A_N)} \quad (3)$$

where U_C and U_N are the fractional abundances of Leu-7 ^{12}CO and Phe-11 ^{14}N, respectively, A_C and A_N are the fractional ^{13}C and ^{15}N natural abundances, respectively, and n is the average number of unlabeled CO sites per peptide strand. For the HFPtr samples, values of U_C, U_N, A_C, A_N, and n are 0.01, 0.01, 0.011, 0.0037, and 29.33, respectively. Equation 3 leads to $(\Delta S/S_0)_i^{\mathrm{cor}}/(\Delta S/S_0)_i^{\exp}$ ratios of ~1.3. The value of σ_i^{cor} was calculated by multiplying $\sigma_i^{\exp}$ by the prefactor for $(\Delta S/S_0)_i^{\exp}$ in eq 3 (*86*).

Simulations. $(\Delta S/S_0)_i^{\mathrm{sim}}$ were calculated as a function of internuclear distances between two or three labeled nuclei and as a function of τ_i. The simulations were done with the SIMPSON program and incorporated the MAS frequency and the ^{13}C and ^{15}N rf fields, pulse lengths, timing, and phases, as well as ^{13}C resonance offsets and CSA principal values and axis directions (*66*). The REDOR simulations were based on a single ^{13}CO/^{15}N spin pair and did not consider the ^{15}N chemical shift or CSA. The fpCTDQBU simulations were based on either two or three ^{13}CO nuclei and did not consider ^{15}N spins. In the experiments, the effects of ^{1}H and ^{14}N spins were largely removed by ^{1}H decoupling, constant-time, and/or MAS, and these spins were not incorporated in any of the simulations.

Orientation-dependent simulation input parameters included ^{13}CO CSA principal values, the Euler angles which relate the ^{13}CO CSA principal axis system(s) to a fixed crystal axis system, and the Euler angles which relate the ^{13}CO−^{15}N or ^{13}CO−^{13}CO internuclear vectors to the crystal axis system. Although distance determination by REDOR and fpCTDQBU experiments is not strongly dependent on these parameters, an effort was made to use reasonable values for the parameters. The (δ_{11}, δ_{22}, δ_{33}) CSA principal values for the *I*4 Ala-9, HFPtr-L7$_C$F11$_N$/PC-PG Leu-7, and HFPtr-L7$_C$F11$_N$/LM3e Leu-7 ^{13}COs were set to (246, 203, 86), (248, 202, 85), and (242, 195, 83) ppm, respectively, and were based on experimentally measured isotropic chemical shifts and literature CSA values (*87*). For GFF, the Gly-1 and Phe-3 CSA principal values were (255, 168, 91) and (243, 193, 106) ppm, respectively, and were determined by fitting experimental centerband and spinning sideband intensities with the Herzfeld−Berger method (*88*).

The Euler angles which relate a ^{13}CO CSA principal axis system to the crystal axis system can be considered in terms of the relative orientation of the principal axis system and the ^{13}CO chemical bonds and the structure and orientation of the molecule relative to the crystal axes. For *I*4 Ala-9, HFPtr Leu-7, and GFF Gly-1 ^{13}COs, the principal axis/chemical bond orientations were (1) the δ_{33} axis perpendicular to the peptide plane and (2) the δ_{22} axis tilted 130° from the CO−N bond (*87*). GFF Phe-3 has COO^- rather than amide functionality, and its δ_{33} axis was perpendicular to the OCO plane and its δ_{11} axis bisected the OCO angle (*89*, *90*).

The crystal frame Euler angles for the ^{13}CO principal axis systems and the internuclear vectors were calculated using a Mathematica program whose inputs were atomic coordinates from high-resolution structures and the previously detailed ^{13}CO CSA principal axis directions. The atomic coordinates for GFF were obtained from its crystal structure while, for parallel β strand and antiparallel β strand structures, coordinates were obtained respectively from the crystal structure of cutinase (PDB file name 1cex) and from the crystal structure of human gamma-D crystalline R58H mutant (PDB file name 1h4a) (*71*, *91*, *92*). The latter two structures have been refined to 1.0 and 1.15 Å resolution, respectively. For REDOR simulations of the *I*4 and HFPtr-

$L7_CF11_N$/PC-PG samples, the Ala-56 CO and Glu-60 N coordinates of cutinase were used. These residues are in a helical region of cutinase, and the labeled ^{13}CO chemical shifts of the two solid-state NMR samples correlate with helical conformation. The REDOR simulation of the HFPtr-$L7_CF11_N$/LM3e sample used coordinates of Leu-114 CO and Gly-118 N in a β strand region of cutinase because the ^{13}CO shift of this sample correlated with β strand conformation. The two-spin fpCTDQBU simulation of the HFPtr-$L7_CF11_N$/LM3e sample used cutinase Ile-37 CO and Ala-116 CO coordinates, and the three-spin fpCTDQBU simulation of the HFPtr-$L7_CF11_N$/LM3e sample used cutinase Ile-37 CO, Ala-116 CO, and Thr-144 CO coordinates. In cutinase, these are in-register residues in a parallel β strand region, and this was our initial structural model for β strand HFPtr.

Signal-to-Noise. Experiments and simulations were carried out to assess the effect of the ^{13}C π rf field on the GFF fpCTDQBU signal-to-noise ratio. Comparison was made between the experimentally based signal-to-noise parameter,

$$\left(\frac{\text{signal}}{\text{noise}}\right)_i^{\text{cor}} = \frac{\left(\frac{\Delta S}{S_0}\right)_i^{\text{cor}}}{\sigma_i^{\text{cor}}} \tag{4}$$

and simulation,

$$\left(\frac{\text{signal}}{\text{noise}}\right)_i^{\text{sim}} = \frac{\left(\frac{\Delta S}{S_0}\right)_i^{\text{sim}}}{\sigma_i^{\text{sim}}} = \frac{\frac{S_{0i}^{\text{sim}} - S_{1i}^{\text{sim}}}{S_{0i}^{\text{sim}}}}{\frac{k}{S_{0i}^{\text{sim}}}\sqrt{1 + \left(\frac{S_{1i}^{\text{sim}}}{S_{0i}^{\text{sim}}}\right)^2}} = \frac{S_{0i}^{\text{sim}} - S_{1i}^{\text{sim}}}{k\sqrt{1 + \left(\frac{S_{1i}^{\text{sim}}}{S_{0i}^{\text{sim}}}\right)^2}} \tag{5}$$

where k is an adjustable parameter to provide overall comparison between $\left(\text{signal/noise}\right)_i^{\text{cor}}$ and $\left(\text{signal/noise}\right)_i^{\text{sim}}$ values for a set of τ_i.

Fitting of Internuclear Distances. The distance between labeled nuclei was determined by χ^2 fitting:

$$\chi^2 = \chi^2(d) = \sum_{i=1}^{T} \frac{\left(\left(\frac{\Delta S}{S_0}\right)_i^{\text{cor}} - \left(\frac{\Delta S}{S_0}(d)\right)_i^{\text{sim}}\right)^2}{(\sigma_i^{\text{cor}})^2} \tag{6}$$

where T is the number of τ_i and d is the dipolar coupling. In units of Å, the ^{13}C$-^{13}$N distance $r_{CN} = (3110\ \text{Hz}/d_{CN})^{1/3}$ and the ^{13}C$-^{13}$C distance $r_{CC} = (7720\ \text{Hz}/d_{CC})^{1/3}$ (*93*). The best-fit d is the one for which χ^2 has global minimum value χ^2_{min} and the uncertainty σ_d is set by the values of d corresponding to $\chi^2 = \chi^2_{\text{min}} + 1$ (*86*). According to statistics theory, the most likely value of χ^2_{min} is the number of degrees of freedom of the fit, ν, and $\nu = T - 1$ in the REDOR and fpCTDQBU analyses (*94*). The χ^2_{min} values in the fittings were close to ν and were consistent with reasonably accurate evaluation of the σ_i^{cor} in eq 6.

RESULTS

^{13}CO Chemical Shifts. Liquid-state and solid-state NMR studies on proteins have shown an empirical correlation between the ^{13}CO chemical shift and local conformation with higher shifts correlating with helical structure and lower shifts correlating with β strand structure (*81*, *95*, *96*). In the present study, ^{13}CO shifts at Leu-7 and Phe-8 were measured for membrane-associated HFPtr and it was observed that there is a strong dependence of shifts on membrane composition. The Phe-8 chemical shift in membrane-associated HFPtr-$F8_CL9_N$ was specifically detected using REDOR filtering (Figure 1a,b), and peak shifts of 178.4 and 172.5 ppm were observed in PC-PG and LM3 membranes, respectively. These values correlate with database distributions of Phe ^{13}CO shifts for helical (177.1 ± 1.4 ppm) and β strand (174.2 ± 1.6 ppm) conformations (*81*). As displayed in Figure 1c, the REDOR-filtered peak Leu-7 ^{13}CO shift in HFPtr-$L7_CF11_N$/PC-PG was 178.8 ppm. This shift agreed better with the database distribution of Leu ^{13}CO in helical conformations (178.5 ± 1.3 ppm) than with the distribution in β strand conformations (175.7 ± 1.5 ppm).

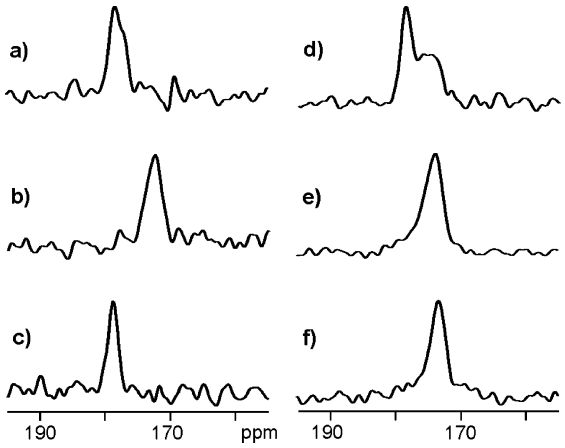

FIGURE 1: ^{13}C spectra of HFPtr-$F8_CL9_N$ associated with (a) PC-PG and (b) LM3 membranes and of HFPtr-$L7_CF11_N$ associated with (c, d) PC-PG, (e) LM3, and (f) LM3e membranes. The HFPtr:lipid mol ratio was ~0.003 in the samples used to obtain spectra a and b and ~0.007 in the samples used to obtain spectra c−f. Spectra a, b, and c are REDOR-filtered with τ_i = 1.0, 1.0, and 32.25 ms, respectively, and have ^{13}CO peak chemical shifts of 178.4 (Phe-8), 172.5 (Phe-8), and 178.8 ppm (Leu-7), respectively. Spectra d, e, and f are REDOR S_0 spectra with 32.25 ms dephasing period and have ^{13}CO peak chemical shifts of 178.6, 173.8, and 173.4 ppm, respectively. Each spectrum was processed with 100 Hz Gaussian line broadening and baseline correction. The MAS frequency was 8000 Hz, and the numbers of scans used to obtain spectra a, b, c, d, e, and f are 118 784, 132 864, 46 048, 23 024, 21 760, and 98 720, respectively.

In the HFPtr-$L7_CF11_N$/LM3 sample, there were relatively small values of $\Delta S/S_0$ and the Leu-7 ^{13}CO peak was not observed in the REDOR-filtered spectrum. REDOR S_0 spectra were therefore used to obtain additional chemical shift information for the HFPtr-$L7_CF11_N$ samples. The S_0 spectrum of the HFPtr-$L7_CF11_N$/PC-PG sample (Figure 1d) is a combination of a sharper signal peaked at 178.6 ppm and a broader signal centered near 176 ppm. Comparison with the REDOR-filtered spectrum (Figure 1c) suggests that the downfield signal is primarily due to the labeled Leu-7 ^{13}CO while spin-counting and published spectra of ^{13}CO labeled lipid samples suggest that the upfield signal is primarily due to natural abundance lipid ^{13}CO (*28*). For the HFPtr-$L7_CF11_N$/LM3 sample (Figure 1e), there is a single signal which is a superposition of intensity from the labeled Leu-7 and natural abundance lipid ^{13}COs with a smaller

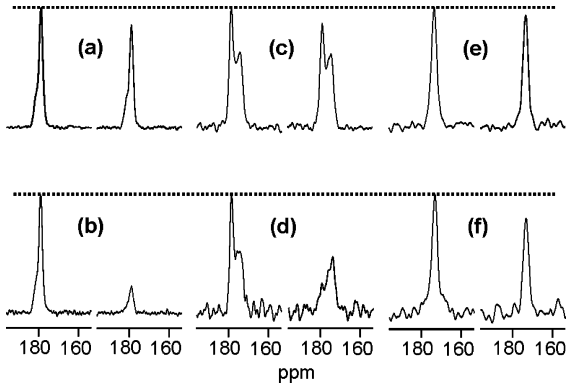

FIGURE 2: ^{13}C REDOR spectra of the (a, b) *I*4 peptide and HFPtr-L7$_C$F11$_N$ associated with (c, d) PC-PG and (e, f) LM3e membranes. For each lettered pair of spectra, the S_0 spectrum is on the left and the S_1 spectrum is on the right. The MAS frequency = 8000 Hz, τ_R = 125 μs, and τ_i = 8.25 ms (spectra a, c, e) or τ_i = 32.25 ms (spectra b, d, f). Dotted lines are drawn at the peak S_0 intensities. The *I*4 spectra were processed with 50 Hz Gaussian line broadening, the HFPtr spectra were processed with 100 Hz Gaussian line broadening, and baseline correction was applied to all spectra. The numbers of scans used to obtain each spectrum in panels a, b, c, d, e, and f are 32, 32, 37 710, 23 024, 40 528, and 98 720, respectively.

contribution from natural abundance HFPtr ^{13}COs. The HFPtr-L7$_C$F11$_N$/LM3e sample contains ether-linked rather than ester-linked lipids with consequent elimination of natural abundance ^{13}CO lipid signals in the spectrum (Figure 1f). The HFPtr-L7$_C$F11$_N$/LM3e spectrum is narrower than the HFPtr-L7$_C$F11$_N$/LM3 spectrum, but the peak shift of the LM3e spectrum (173.4 ppm) is very similar to the peak shift of the LM3 spectrum (173.8 ppm) and suggests that the HFPtr conformation is insensitive to ether- vs ester-linked lipids. The peak shifts are more consistent with Leu chemical shifts in β strand conformations (175.7 ± 1.5 ppm) than in helical conformations (178.5 ± 1.3 ppm).

Overall, the Leu-7 and Phe-8 peak HFPtr ^{13}CO chemical shifts correlate with local helical conformation in PC-PG and with β strand conformation in LM3 and LM3e. Other studies of HIV and influenza fusion peptides suggest that the absence of cholesterol in PC-PG and its presence in LM3 and LM3e are important determinants of peak chemical shifts and local conformations (*27*, *76*).

^{13}CO−^{15}N Distances. HFPtr-L7$_C$F11$_N$ conformation was probed more quantitatively with REDOR determination of the distance between the labeled Leu-7 ^{13}CO and Phe-11 ^{15}N nuclei. If the Leu-7 to Phe-11 region has regular α helical conformation, the distance will be ∼4.1 Å while if the region has regular β strand conformation, the distance will be ∼11 Å. These distances correspond to dipolar couplings (d_{CN}) of ∼45 Hz and ∼3 Hz, respectively.

The REDOR experiment was first validated using the helical *I*4 peptide with Ala-9 ^{13}CO and Ala-13 ^{15}N labels (Figure 2a,b and Figure 3). As τ_i was increased from 8.25 to 32.25 ms, there was a regular decrease in $S_{1i}^{exp}/S_{0i}^{exp}$ values and concomitant increase in $(\Delta S/S_0)_i^{exp}$ values. Using the approach and equations described in Materials and Methods and the Supporting Information, the $(\Delta S/S_0)_i^{cor}$ were calculated from the $(\Delta S/S_0)_i^{exp}$ and then fitted to the $(\Delta S/S_0)_i^{sim}$ calculated for an array of d_{CN} values. The resulting d_{CN} = 44.78 ± 0.22 Hz and r_{CN} = 4.110 ± 0.007 Å are consistent with α helical structure between Ala-9 and Ala-13 and serve to validate the REDOR experiment.

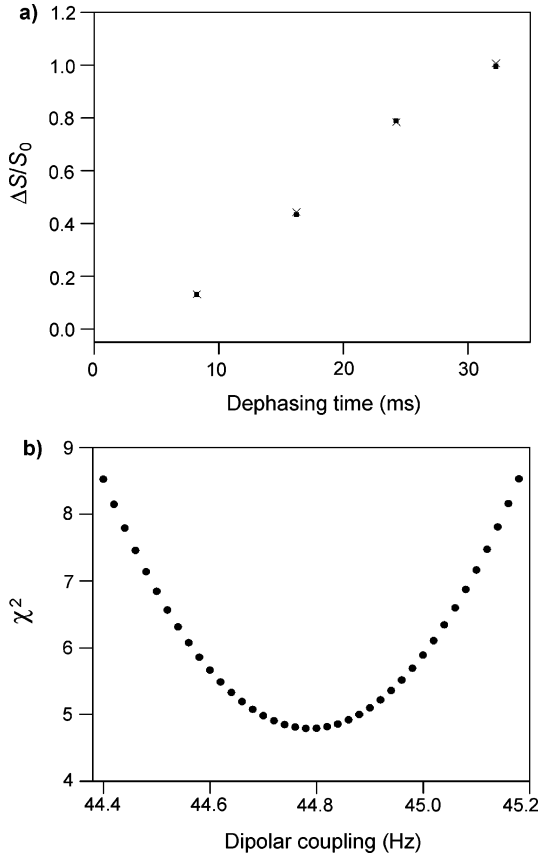

FIGURE 3: (a) REDOR $(\Delta S/S_0)_i^{cor}$ (filled squares) and $(\Delta S/S_0)_i^{sim}$ (crosses) vs dephasing time for the *I*4 peptide. Each $(\Delta S/S_0)_i^{cor}$ was based on a $(S/S_0)_i^{exp}$ determined by integrations of 1 ppm regions in the S_0 and S_1 spectra. The integration region was centered at 178.8 ppm, which is the peak shift in the S_0 spectra. For each τ_i, there were 64 total ($S_0 + S_1$) scans. The values of σ_i^{cor} are ∼0.005, and the heights of the black squares are approximately equal to the average value of 2 × σ_i^{cor}. (b) A plot of χ^2 vs d_{CN} yields d_{CN} = 44.78 ± 0.22 Hz, which corresponds to r_{CN} = 4.110 ± 0.007 Å for the Ala-9 ^{13}CO/Ala-13 ^{15}N labeled pair. The uncertainty was determined using the approach described in Materials and Methods. The $(\Delta S/S_0)_i^{sim}$ values in plot a were calculated with the best-fit d_{CN}.

REDOR experiments were then performed on the HFPtr-L7$_C$F11$_N$/PC-PG sample. For the Leu-7 ^{13}CO peak at 178.6 ppm, spectra with τ_i at 8.25 and 32.25 ms yielded $S_{1i}^{exp}/S_{0i}^{exp}$ values which were in semiquantitative agreement with the $S_{1i}^{exp}/S_{0i}^{exp}$ values from the *I*4 sample (Figure 2a−d). In the HFPtr spectra, the upfield natural abundance lipid ^{13}CO signals near 175 ppm have $(S_{1i}^{exp}/S_{0i}^{exp}) \sim 1$ for all τ_i, which is consistent with the expected large ^{13}CO−^{15}N distances and corresponding small d_{CN} values for these nuclei. Fitting of the Leu-7 $(\Delta S/S_0)_i^{cor}$ to $(\Delta S/S_0)_i^{sim}$ yielded d_{CN} = 44.8 ± 2.4 Hz and r_{CN} = 4.11 ± 0.08 Å for the Leu-7 ^{13}CO/Phe-11 ^{15}N labeled pair (Figure 4). These values are consistent with α helical structure between the labeled nuclei and correlate with the previously discussed downfield Leu-7 ^{13}CO chemical shift.

REDOR spectra of the HFPtr-L7$_C$F11$_N$/LM3e sample yielded $S_{1i}^{exp}/S_{0i}^{exp}$ values which were significantly smaller than the $S_{1i}^{exp}/S_{0i}^{exp}$ values for the *I*4 sample and suggest that the region between Leu-7 and Phe-11 has nonhelical conformation (Figure 2a,b,e,f). Fitting of $(\Delta S/S_0)_i^{cor}$ to $(\Delta S/S_0)_i^{sim}$ yielded d_{CN} = 15.8 ± 1.8 Hz, which corresponds to

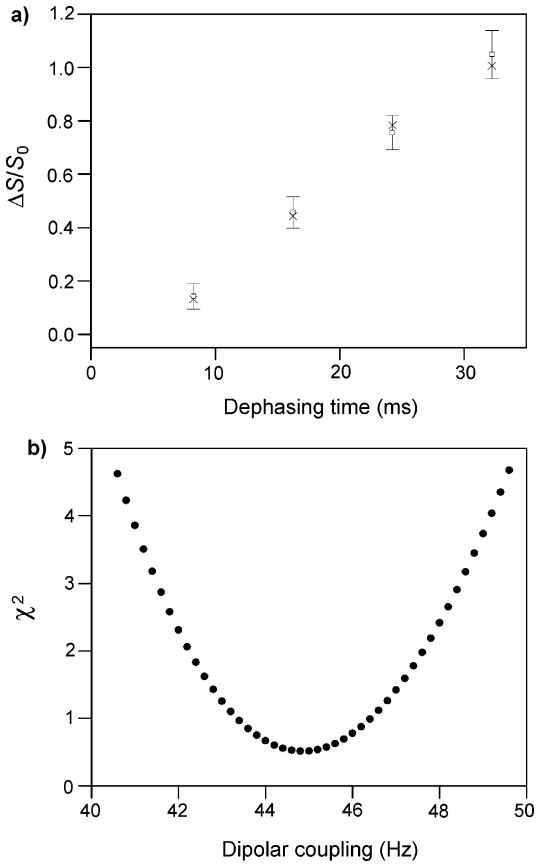

FIGURE 4: (a) REDOR $(\Delta S/S_0)_i^{cor}$ (open squares with error bars) and $(\Delta S/S_0)_i^{sim}$ (crosses) vs dephasing time for the HFPtr-L7$_C$-F11$_N$/PC-PG sample. Each $(\Delta S/S_0)_i^{cor}$ was based on a $(\Delta S/S_0)_i^{exp}$ determined from spectral integrations over a 1 ppm region centered at 178.6 ppm, the Leu-7 ^{13}CO peak chemical shift. The total ($S_0 + S_1$) numbers of scans used to obtain the $(\Delta S/S_0)_i^{cor}$ values for τ_i = 8.25, 16.25, 24.25, and 32.25 ms were 75 420, 52 832, 41 568, and 46 048, respectively. (b) A plot of χ^2 vs d_{CN} yields $d_{CN} = 44.8 \pm 2.4$ Hz, which corresponds to $r_{CN} = 4.11 \pm 0.08$ Å for the Leu-7 ^{13}CO/Phe-11 ^{15}N labeled pair. The $(\Delta S/S_0)_i^{sim}$ values in plot a were calculated with the best-fit d_{CN}.

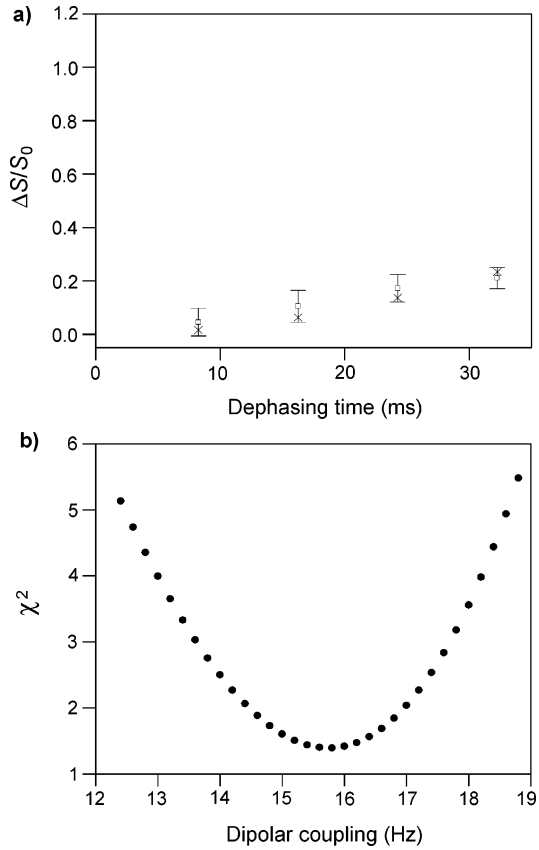

FIGURE 5: (a) REDOR $(\Delta S/S_0)_i^{cor}$ (open squares with error bars) and $(\Delta S/S_0)_i^{sim}$ (crosses) vs dephasing time for the HFPtr-L7$_C$-F11$_N$/LM3e sample. Each $(\Delta S/S_0)_i^{cor}$ was based on a $(\Delta S/S_0)_i^{exp}$ determined from spectral integrations over a 1 ppm region centered at 173.4 ppm, the peak shift in the S_0 spectra. The total ($S_0 + S_1$) numbers of scans used to obtain the $(\Delta S/S_0)_i^{cor}$ values for τ_i = 8.25, 16.25, 24.25, and 32.25 ms were 81 056, 76 288, 172 512, and 197 440, respectively. (b) A plot of χ^2 vs d_{CN} yields $d_{CN} = 15.8 \pm 1.8$ Hz, which corresponds to $r_{CN} = 5.8 \pm 0.3$ Å for the Leu-7 ^{13}CO/Phe-11 ^{15}N labeled pair. The $(\Delta S/S_0)_i^{sim}$ values in plot a were calculated with $d_{CN} = 15.8$ Hz.

$r_{CN} = 5.8 \pm 0.3$ Å for the Leu-7 ^{13}CO/Phe-11 ^{15}N labeled pair (Figure 5). This distance is longer than the ~4.1 Å distance expected in an α helical conformation and shorter than the ~11 Å distance expected in a β strand conformation. This result is discussed after presentation of the fpCTDQBU analyses; briefly, structural models suggest that the REDOR data reflect an interpeptide distance and provide information about the register of residues in adjacent β strands.

^{13}CO−^{13}CO Distances. An in-register parallel β strand model for the HFPtr-L7$_C$F11$_N$/LM3e sample was tested with fpCTDQBU measurements of adjacent interstrand Leu-7 ^{13}CO/Leu-7 ^{13}CO dipolar couplings and distances. If the model is correct, the distance will be ~4.8 Å with $d_{CC} \sim 70$ Hz.

The fpCTDQBU experiment was first validated using the GFF sample for which there is a ~2% fraction of D-GFF molecules with ^{13}CO labels at Gly-1 and Phe-3. D-GFF has an intramolecular ^{13}CO/^{13}CO distance of 5.40 Å and $d_{CC} \sim 49$ Hz. The GFF fpCTDQBU spectra have Phe-3, Phe-2 and Gly-1 ^{13}CO peaks at 180.3, 176.4, and 170.9 ppm, respectively (Figure 6a−d). As τ_i was increased from 16 to 80 ms, there was a general decrease in $S_{1i}^{exp}/S_{0i}^{exp}$ values for the Phe-3 and Gly-1 peaks. This is consistent with the 65% contribution to these signals from D-GFF molecules for which there is significant Gly-1 ^{13}CO/Phe-3 ^{13}CO dipolar coupling. By contrast, the Phe-2 peak has $S_{1i}^{exp}/S_{0i}^{exp} \sim 1$ for all τ_i, which is consistent with the ~98% contribution to this signal from unlabeled GFF molecules for which there are large ^{13}CO/^{13}C distances and corresponding small d_{CC} values.

As the magnitude of the constant-time parameter increases, transverse relaxation causes a decrease in ^{13}CO signal intensity for all values of τ_i and consequent lower signal-to-noise ratio. It was therefore desirable to use the smallest constant-time which allowed observation of the full $(\Delta S/S_0)_i$ buildup for a ~5 Å ^{13}CO−^{13}CO distance. Because RFDR is affected by ^{13}C pulse duration, an investigation was made of the effect of the ^{13}C π pulse rf field on the $(\Delta S/S_0)_i$ buildup rate and signal-to-noise ratio of the GFF sample (*65*). For the Gly-1 ^{13}CO signal, smaller ^{13}C π pulse rf fields yielded faster buildup in both experiment and simulation (Figure 7a) but also led to smaller S_0 and S_1 signal intensities, perhaps because of larger resonance offsets and poorer refocusing of chemical shift evolution. A ^{13}C π pulse rf field of ~10 kHz gave the best overall $(\Delta S/S_0)_i$ buildup rate and signal-to-noise ratio (Figure 7b). Good agreement between (ΔS/

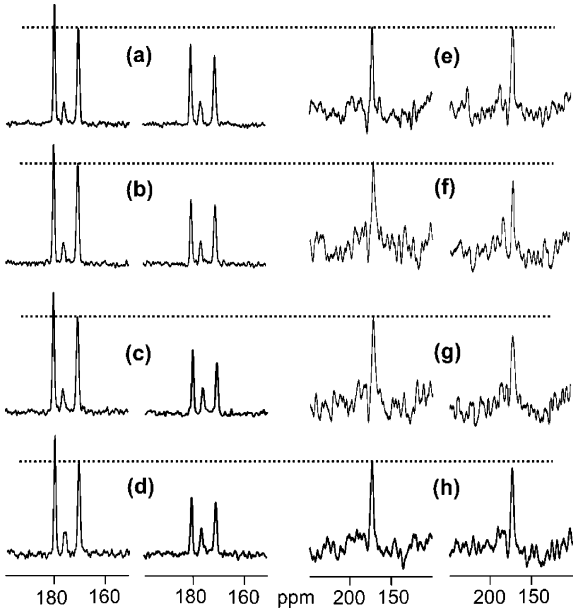

FIGURE 6: fpCTDQBU spectra of (a−d) the GFF sample and (e−h) the HFPtr-L7$_C$F11$_N$/LM3e sample. For each lettered pair of spectra, the S_0 spectrum is on the left and the S_1 spectrum is on the right. The MAS frequency = 8000 Hz, τ_R = 125 μs, the ^{13}C π pulse rf field = 10 kHz, M = 336, and the total constant-time = $(L + M + N) \times \tau_R$ = 84 ms. The values of L, N, and τ_i are 128, 208, 32 ms (spectra a, e); 192, 144, 48 ms (spectra b, f); 256, 80, 64 ms (spectra c, g); 320, 16, 80 ms (spectra d, h). From left to right, each GFF spectrum has Phe-3, Phe-2, and Gly-1 ^{13}CO peaks at 180.3, 176.4, and 170.9 ppm, respectively. For each set of GFF and HFPtr spectra with the same τ_i, a dotted line is drawn at the peak S_0 intensities of Gly-1 (GFF) and Leu-7 (HFPtr). The GFF spectra were processed with 50 Hz Gaussian line broadening, the HFPtr spectra were processed with 250 Hz Gaussian line broadening, and baseline correction was applied to all spectra. For some of the HFPtr spectra, there is a small glitch at ~178 ppm which is due to DC offset in the data. The total numbers of scans used to obtain each spectrum in panels a, b, c, d, e, f, g, and h are 10 240, 10 240, 10 240, 8192, 77 056, 80 736, 102 432, and 152 064, respectively.

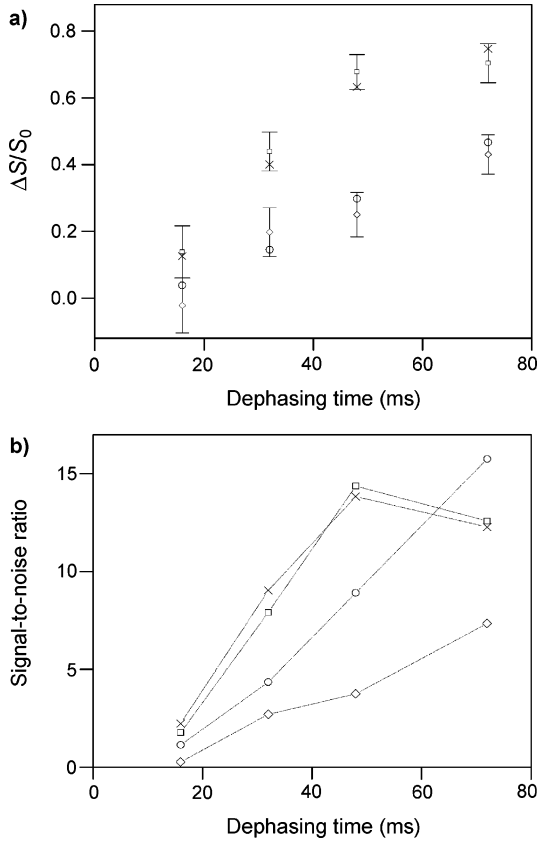

FIGURE 7: Dependence of fpCTDQBU of GFF Gly-1 ^{13}CO on ^{13}C π pulse rf field: (a) $(\Delta S/S_0)_i^{cor}$ and $(\Delta S/S_0)_i^{sim}$ vs dephasing time; and (b) signal-to-noise ratio of $(\Delta S/S_0)_i^{cor}$ and $(\Delta S/S_0)_i^{sim}$ vs dephasing time. The MAS frequency = 8000 Hz, $\delta^{13}_{C\ transmitter}$ = 175.7 ppm, M = 336, and the constant-time = 84 ms. The symbol legend is as follows: squares, cor, 10 kHz ^{13}C π pulse rf field; crosses, sim, 10 kHz field; diamonds, cor, 43 kHz field; circles, sim, 43 kHz field. Uncertainties are displayed for the cor points in plot a, and lines are drawn between like symbols in plot b. Each $(\Delta S/S_0)_i^{cor}$ was based on a $(S/S_0)_i^{exp}$ determined from spectral integrations over a 0.5 ppm region centered at the Gly-1 ^{13}CO peak chemical shift. Each $(\Delta S/S_0)_i^{cor}$ value was determined using intensities from 4096 total $(S_0 + S_1)$ scans. The S_{0i}^{sim} and S_{1i}^{sim} were calculated with d_{CC} = 42 Hz which yielded the best overall agreement between $(\Delta S/S_0)_i^{cor}$ and $(\Delta S/S_0)_i^{sim}$ values. The value of k (eq 5) was set to give the best agreement at 10 kHz field between the sim and cor signal-to-noise ratios.

$S_0)_i^{cor}$ and $(\Delta S/S_0)_i^{sim}$ at 10 and 43 kHz fields was obtained using d_{CC} = 42 Hz. Good agreement between experimental and simulated signal-to-noise ratios at 10 kHz field was obtained using a single value of k (eq 5) while at 43 kHz field, this k value resulted in simulated signal-to-noise ratios about double those observed in experiment. Because the ^{13}C π pulses at 43 kHz field are shorter than those at 10 kHz field, the 43 kHz experimental pulses are more poorly approximated by the ideal rectangular pulses of the simulations. This may result in poorer refocusing performance of the 43 kHz experimental ^{13}C π pulses and lower signal-to-noise ratios relative to simulation.

Subsequent fpCTDQBU experiments were done with a 10 kHz ^{13}C π pulse rf field. Figure 8 displays comparison and fitting of GFF Gly-1 ^{13}CO $(\Delta S/S_0)_i^{cor}$ and $(\Delta S/S_0)_i^{sim}$ over a wide range of τ_i. The analysis focused on Gly-1 ^{13}CO because it has carbonyl rather than carboxyl functionality and is thus more relevant to the HFPtr sample. The fitting yielded d_{CC} = 42.3 ± 0.5 Hz and corresponding r_{CC} = 5.67 ± 0.02 Å for the Gly-1 ^{13}CO/Phe-3 ^{13}CO labeled pair. Variation of ^{13}CO CSA axis orientations relative to the GFF atomic geometry did not greatly affect $(\Delta S/S_0)_i^{sim}$ and the fitted values of d_{CC}. For example, different sets of $(\Delta S/S_0)_i^{sim}$ were calculated with each set having a randomly generated principal axis orientation. Each set of $(\Delta S/S_0)_i^{sim}$ was then fitted to $(\Delta S/S_0)_i^{cor}$, and the resulting d_{CC} was always within a range of 37−47 Hz.

In Figure 8a, the only systematic disagreement between $(\Delta S/S_0)_i^{cor}$ and $(\Delta S/S_0)_i^{sim}$ occurs at large values of τ_i for which $(\Delta S/S_0)_i^{cor}$ decreases more rapidly than $(\Delta S/S_0)_i^{sim}$. The best-fit r_{CC} is ~5% larger than the 5.40 Å crystallographic distance (*71*). Uncertainty in the D-GFF:unlabeled GFF ratio in the sample is one possible reason for this discrepancy because this ratio affects the $(\Delta S/S_0)_i^{exp} \rightarrow (\Delta S/S_0)_i^{cor}$ conversion (cf. Materials and Methods and Supporting Information). The potential effect of this uncertainty was tested by calculation of $(\Delta S/S_0)_i^{sim}$ with d = 49 Hz (r_{CC} = 5.40 Å) and then fitting $(\Delta S/S_0)_i^{cor}$ to $(\Delta S/S_0)_i^{sim}$ as a function of the D-GFF:unlabeled GFF ratio (Figure 8c). Good fits were obtained with ratios of ~1:70 which is close to the ratio of 1:50 derived from weights of D-GFF and unlabeled GFF in the sample and by the ratio of the Gly-

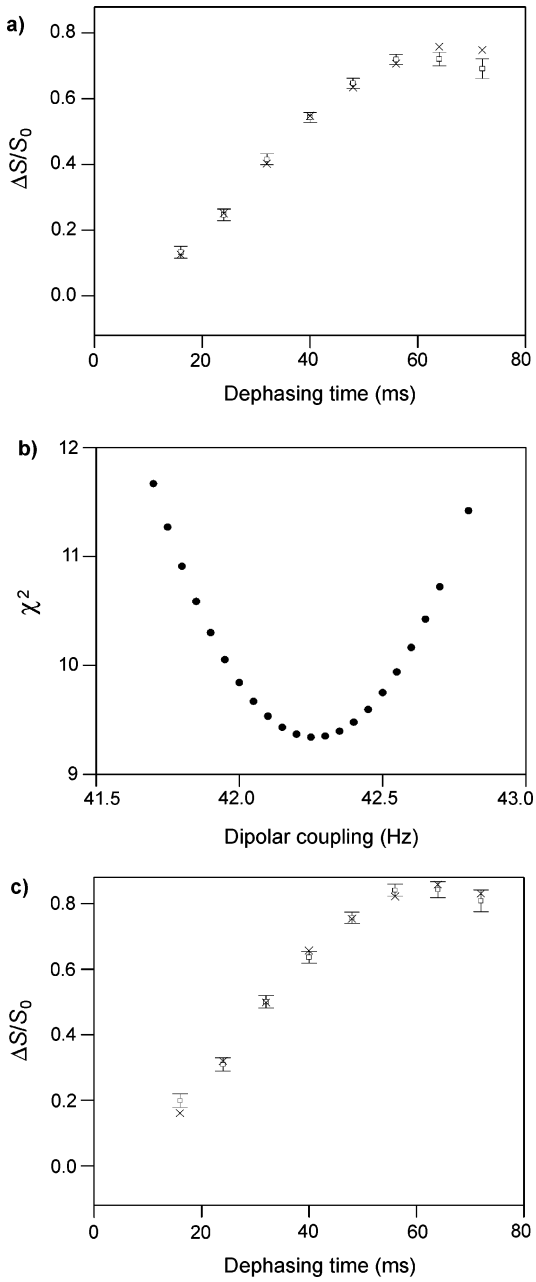

FIGURE 8: (a) fpCTDQBU $(\Delta S/S_0)_i^{cor}$ (open squares with error bars) and $(\Delta S/S_0)_i^{sim}$ (crosses) vs dephasing time for GFF Gly-1 ^{13}CO. The MAS frequency = 8000 Hz, the ^{13}C π pulse rf field = 10 kHz, $\delta_{^{13}\text{C transmitter}} = 175.7$ ppm, $M = 336$, and the constant-time = 84 ms. Each $(\Delta S/S_0)_i^{cor}$ was based on a $(\Delta S/S_0)_i^{exp}$ determined from spectral integrations over a 0.5 ppm region centered at the Gly-1 ^{13}CO peak chemical shift. Each $(\Delta S/S_0)_i^{cor}$ value for $\tau_i = 16$, 24, 32, 40, 48, 56, and 64 ms was determined using intensities from 20 480 total $(S_0 + S_1)$ scans, and the $(\Delta S/S_0)_i^{cor}$ value for $\tau_i = 72$ ms was determined using intensities from 16 384 total scans. (b) A plot of χ^2 vs d_{CC} yields $d_{CC} = 42.3 \pm 0.5$ Hz, which corresponds to $r_{CC} = 5.67 \pm 0.02$ Å for the Gly-1/Phe-3 labeled pair. The $(\Delta S/S_0)_i^{sim}$ values in panel a were calculated with $d = 42.3$ Hz. (c) Plot of $(\Delta S/S_0)_i^{cor}$ (open squares with error bars) and $(\Delta S/S_0)_i^{sim}$ (crosses) calculated with $d_{CC} = 49$ Hz, which corresponds to $r_{CC} = 5.40$ Å, the Gly-1 CO/Phe-3 CO distance in the X-ray structure. The $(\Delta S/S_0)_i^{cor}$ were fitted to $(\Delta S/S_0)_i^{sim}$ as a function of the D-GFF: unlabeled GFF ratio, and the displayed $(S/S_0)_i^{cor}$ were calculated with the best-fit value of the ratio (1:71) for which $\chi^2 = 7$.

1:Phe-2 ^{13}CO intensities. Overall, the GFF studies demonstrate that ^{13}C−^{13}C distances in the ∼5 Å range can be reasonably accurately determined with the fpCTDQBU method.

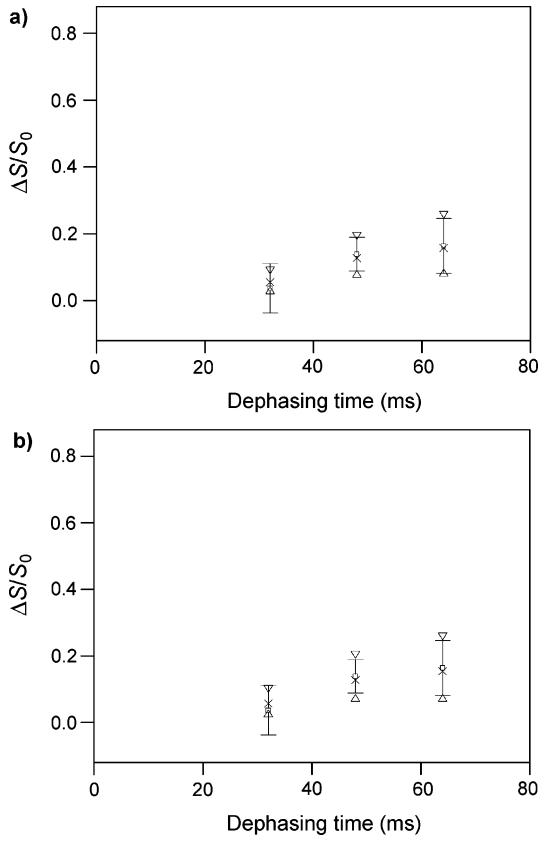

FIGURE 9: fpCTDQBU $(\Delta S/S_0)_i^{cor}$ and $(\Delta S/S_0)_i^{sim}$ vs dephasing time for the HFPtr-L7$_C$F11$_N$/LM3e sample. The MAS frequency = 8000 Hz, the ^{13}C π pulse rf field = 10 kHz, $\delta_{^{13}\text{C transmitter}} = 178.4$ ppm, $M = 336$, and the constant-time = 84 ms. The $(\Delta S/S_0)_i^{cor}$ values are open squares with error bars. Each $(\Delta S/S_0)_i^{cor}$ was based on a $(\Delta S/S_0)_i^{exp}$ determined from spectral integrations over a 1 ppm region centered at 173.4 ppm, the peak shift in the S_0 spectra. The total $(S_0 + S_1)$ numbers of scans used to obtain the $(\Delta S/S_0)_i^{cor}$ values for $_i$ = 32, 48, and 64 ms were 154 112, 161 472, and 204 864, respectively. The $(\Delta S/S_0)_i^{sim}$ values were calculated with two-spin and three-spin models in plots a and b, respectively. In plot a, the up triangles, crosses, and down triangles correspond to $d_{CC} = 10$, 15, and 20 Hz, respectively, and in plot b, they correspond to $d_{CC} = 8$, 13, and 18 Hz, respectively. The best-fit values of d_{CC} are ∼15 Hz and ∼13 Hz for the two-spin and three-spin models, respectively, and correspond to interstrand Leu-7 ^{13}CO−^{13}CO distances of 8.0 Å and 8.4 Å. Reasonable upper limits on d_{CC} in the two-spin and three-spin models are ∼20 Hz and ∼18 Hz respectively, and correspond to distances of 7.3 Å and 7.5 Å.

The fpCTDQBU spectra of the HFPtrL7$_C$F11$_N$/LM3e sample are displayed in Figure 6e−h. Relative to the Gly-1 and Phe-3 ^{13}CO peaks in the GFF spectra (Figure 6a−d), the HFPtr spectra have larger S_{1i}/S_{0i} ratios which are consistent with a d_{CC} smaller than in D-GFF and a Leu-7 ^{13}CO/Leu-7 ^{13}CO distance longer than that in D-GFF. The $\tau_i = 32$, 48, and 64 ms points were fitted in the context of a "two-spin" or a "three-spin" model (Figure 9). The 80 ms point was not included in the fitting because of the systematic disagreement between $(\Delta S/S_0)_i^{cor}$ and $(\Delta S/S_0)_i^{sim}$ at large values of τ_i in the GFF analysis (Figure 8a). The two-spin (three-spin) model has two (three) adjacent in-register parallel β strands, and the simulations are based on two (three) ^{13}COs, each of which is at the same residue position in its respective strand. The interstrand distance and corresponding d_{CC} value

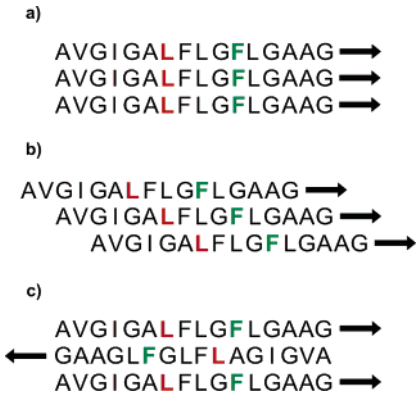

FIGURE 10: Structural models for strand arrangements of LM3e-associated HFPtr: (a) parallel in-register; (b) parallel with adjacent strands two residues out-of-register; and (c) antiparallel with adjacent strand crossing between Phe-8 and Leu-9. The first sixteen residues of each strand are displayed, the ^{13}CO labeled Leu-7 are colored red, and the ^{15}N labeled Phe-11 are colored green.

were input parameters for the simulations. In the three-spin model, the two outside strands were always equidistant from the central strand.

The fitting is based on three points with relatively large uncertainties, and visual comparison was used to assess best-fit d and its uncertainty. The best-fit values of d_{CC} in the two-spin and three-spin models are ~15 Hz and ~13 Hz, respectively, and correspond to r_{CC} of 8.0 Å and 8.4 Å. Reasonable upper limits on d_{CC} in the two-spin and three-spin models are ~20 Hz and ~18 Hz, respectively, and correspond to r_{CC} of 7.3 Å and 7.5 Å. The lower limits on d_{CC} and upper limits on r_{CC} are more difficult to assess because of the uncertainties in $(\Delta S/S_0)_i^{cor}$ and weak dependence of $(\Delta S/S_0)_i^{sim}$ on d_{CC} at small values of d_{CC}. Overall, experimental values of d_{CC} and r_{CC} do not support the in-register parallel β model for which d_{CC} ~ 70 Hz and r_{CC} ~ 4.8 Å.

Strand Arrangement Models. Figure 10 displays three models: (a) parallel β strand with all strands in-register; (b) parallel β strand with adjacent strands two residues out-of-register; and (c) antiparallel β strand with adjacent strand crossing between Phe-8 and Leu-9. Each model is shown with three strands although we do not have information about the numbers of strands in the LM3e-associated HFPtr oligomer. Table 1 displays Leu-7 CO/Phe-11 N and interstrand Leu-7 CO/Leu-7 CO distances from REDOR and fpCTDQBU experiments and from the models. The model distances are averages for parallel strand regions of cutinase and antiparallel strand regions of human gamma-D crystalline R58H mutant whose crystal structures have been refined to 1.0 Å and 1.15 Å, respectively (*91*, *92*).

There are significant differences between the experimental distances and in-register parallel strand model distances. The experimental Leu-7 ^{13}CO/Phe-11 ^{15}N distance is ~6 Å, which is much shorter than the ~11 Å intrastrand or interstrand distance in the model. The lower limit on the experimental interstrand Leu-7 ^{13}CO/Leu-7 ^{13}CO distance is >7 Å and is significantly longer than the 4.8 Å distance in the model.

Distances in the out-of-register parallel strand and antiparallel strand models are more consistent with the experimentally derived distances. There are ~6 Å interstrand Leu-7 CO/Phe-11 N distances because of the strand registers in the models. In addition, the interstrand Leu-7 CO/Leu-7 CO distances are ~8 Å. Calculations of REDOR and fpCTDQBU $(\Delta S/S_0)_i^{sim}$ for the two models agreed reasonably well with $(\Delta S/S_0)_i^{cor}$. The data were more poorly fit by other strand arrangement models.

Table 1: Experimental and Model Distances[a]

	r_{CN} (Å)[b]	r_{CC} (Å)[c]
experiment	5.8 (3)	8.2 (9)
parallel in-register model[d]	11.0 (3)	4.8 (2)
parallel out-of-register model[e]	6.5 (3)	8.2 (3)
antiparallel model[f]	6.1 (3)	8.5 (3)

[a] Each model distance was determined from a region of a high-resolution crystal structure which has the same strand arrangement as the model. Several interatomic distances were measured in this region. An average distance is reported in the table as well as the standard deviation in units of 0.1 Å in parentheses. [b] Leu-7 CO/Phe-11 N distance. [c] Interstrand Leu-7 CO/Leu-7 CO distance. [d] Model distances were determined from the region of the cutinase protein corresponding to residues 34−39, 113−120, and 143−148. [e] Adjacent strands are two residues out-of-register. Model distances were determined from the cutinase protein. [f] Adjacent strands cross between Phe-8 and Leu-9. Model distances were determined from the region of the human gamma-D crystalline R58H mutant protein corresponding to residues 2−7, 14−18, and 34−38.

Further experiments are required to distinguish between the two models. For example, we recently observed Ala-6 ^{13}C/Gly-10 ^{13}C cross-peaks in 2D spectra of LM3-associated HFP which was uniformly ^{13}C labeled at Ala-6 and Gly-10 (*97*). The cross-peaks were generated by magnetization exchange due to proton-driven spin diffusion which typically occurs between ^{13}C nuclei separated by <6 Å. For the out-of-register parallel and antiparallel models, the closest distance between Ala-6 and Gly-10 ^{13}C atoms is ~7.1 Å and ~4.5 Å, respectively, and the spectra are more consistent with the antiparallel model. Future experiments could be based on the REDOR approaches used to recently elucidate strand arrangements in the PG-1 antimicrobial peptide (*59*).

A turn structure in the Leu-7 to Phe-11 region could also be consistent with the experimental Leu-7 CO/Phe-11 N distance. Although this possibility cannot be definitively ruled out, measurements of ^{13}C chemical shifts for nuclei in this region of LM3-associated HFP are all consistent with β strand conformation (*29*, *97*). We also note the possibility of populations of distinct strand arrangements which would necessitate fitting REDOR and fpCTDQBU signals with populations of distinct spin geometries.

In summary, the REDOR and fpCTDQBU data are consistent with a parallel strand arrangement with adjacent strands two residues out-of-register and with an antiparallel arrangement whose adjacent strand crossing is between Phe-8 and Leu-9. The data are not consistent with an in-register parallel strand arrangement.

DISCUSSION

Conformational Plasticity. The structural plasticity of membrane-associated viral fusion peptides has been observed by several groups using a variety of experimental probes, and it is known that they can exist in helical or nonhelical forms (*7*). Other investigators have developed structural models for the helical form of the peptides based principally on liquid-state NMR, ESR, and IR data (*33*, *38*, *39*, *73*, *74*). IR and solid-state NMR studies of the β strand form of HFP and its oligomeric constructs have shown parallel strand

arrangement, antiparallel strand arrangement, and a mixture of parallel and antiparallel arrangements (*26*, *43*, *44*). In the present study, the structure of membrane-associated HFPtr was explored with solid-state NMR methods including chemical shift, heteronuclear distance, and homonuclear distance measurements. The data suggest that the region of HFPtr between Leu-7 and Phe-11 is α helical when associated with membranes without cholesterol and is β strand when associated with membranes which have a lipid headgroup and cholesterol composition similar to that of host cells of the virus. These results are consistent with our observations that, for a single FP:lipid mol ratio, cholesterol favors formation of the β strand conformation of fusion peptides (*27*, *76*, W. Qiang and D. P. Weliky, unpublished experiments). This conformational difference has been seen both at room temperature and at the −50 °C temperature of the experiments in this paper (*29*). The observed fusion peptide conformations appear to be equilibrium rather than kinetically trapped structures (*98*).

The presence of cholesterol in membranes is known to increase the lateral molecular packing density and membrane tensile strength, decrease in-plane elasticity and permeability of water through the membrane, and promote formation of the "liquid-ordered phase" (*99*−*104*). This phase is characterized by a rapid lateral molecular translational diffusion coefficient similar to that of the "liquid-disordered" phase and high configurational order of the lipid acyl chains similar to that of the "solid-ordered" phase (*104*, *105*). These latter phases exist for non-cholesterol-containing membranes at higher and lower temperature, respectively. Fluorescence data suggest that HFPmn in its helical form inserts more deeply into the membrane than HFPmn in its β strand form (*106*). The higher molecular packing density in the cholesterol-containing membranes may make HFPtr insertion more difficult and thus favor a more surface-associated β strand form.

Because the rapid fusion rate of HFPtr is observed both for vesicles which contain cholesterol and for vesicles which do not contain cholesterol, one reasonable hypothesis is that both the helical and β strand structures of HFPtr are highly fusogenic (*46*). Other investigators have proposed that the peptide structure responsible for fusion is irregular and may be transient (*107*, *108*). Although the present paper does not directly address these issues, it is noted that (1) cholesterol-associated structural variation is also observed for the influenza virus fusion peptide (*27*, *76*) and (2) pH-triggered fusion can be observed both for helical influenza fusion peptide bound to non-cholesterol-containing membranes and for β strand influenza fusion peptide bound to cholesterol-containing membranes (*109*). These results argue in favor of fusogenic activity of both helical and β strand structures. Lentz and co-workers have proposed that fusion peptides catalyze fusion by filling void spaces in nonbilayer fusion intermediates and that this function can be done by peptides in either helical or β strand conformation (*110*). Our results are consistent with this model, and two fusogenic conformations may allow the virus to fuse with a wider variety of membrane compositions. Membranes of uninfected host cells of HIV contain ∼30 mol % cholesterol, and there is some depletion of cholesterol in these membranes after HIV infection (*77*, *78*). The HIV membrane contains ∼45 mol % cholesterol, and there is some evidence that HIV fuses with cholesterol-rich regions of host cell membranes (*111*).

The 15−40-fold higher rate of HFPtr-induced lipid mixing relative to HFPmn is observed both with PC-PG vesicles for which the final HFPtr conformation is helical and with LM3 vesicles for which the final conformation is β strand. For either conformation, there is a higher local concentration of peptide strands at the membrane surface with HFPtr than with HFPmn, and this larger concentration could cause greater perturbation of the membrane and provide a general model for the increased fusion rate of HFPtr. Other possible differences between HFPtr and HFPmn are their depths and angles of membrane insertion as well as the arrangement and interactions of individual helices or strands.

Strand Arrangement. Previous solid-state NMR REDOR data for HFPmn associated with cholesterol-containing membranes were consistent with a mixture of parallel and antiparallel strand arrangements (*43*). A predominant parallel strand arrangement is an appealing structural model to explain the increased fusion rate of β strand HFPtr because it places the apolar N-terminal regions of the strands close to one another and thereby provides a larger apolar volume to perturb the membrane. The solid-state NMR data of this paper are consistent with a parallel model with adjacent strands two residues out of register.

The data are also consistent with antiparallel strands with adjacent strands crossing between Phe-8 and Leu-9. For this antiparallel arrangement, the sixteen N-terminal apolar residues (Ala-1 to Gly-16) could form a hydrogen-bonded β strand oligomer and the more polar C-terminal residues would be outside the hydrogen-bonded oligomer. If residues Ala-1 to Gly-16 form a single β strand without turns, then a structural building block could be based on two HFPtr molecules "A" and "B". The A_1, A_2, and A_3 strands would run in the same direction (as enforced by the cross-linking), and the B_1, B_2, and B_3 strands would run in the opposite direction. An antiparallel interleaved arrangement could be $A_1B_3A_2B_2A_3B_1$; i.e. residues in strand B_3 are hydrogen bonded to residues in strands A_1 and A_2. This antiparallel structure would place the bulky C-terminal regions of the HFPtr molecules on either side of the oligomer and could allow more efficient assembly of multiple HFPtr trimers at the membrane surface with consequent greater membrane perturbation and fusion rate. The total number of strands in a hydrogen-bonded oligomer may not be large as evidenced by poor room-temperature cross-polarization and the inferred high molecular mobility (*29*).

For membrane-associated HFPmn, IR data from several groups support an antiparallel strand arrangement (*26*, *30*, *110*, *112*). However, IR data on constructs which contain the first 34 or 70 residues of gp41 support an in-register parallel strand arrangement (*44*). These latter constructs contain the 23 residues of HFPmn as well as an additional 11 or 47 C-terminal residues. The variation in strand arrangements among the constructs may be due to sequence or cross-linking differences (*113*).

Accurate Measurement of Weak Couplings. Model compound results in this paper provide insight into the accuracy with which solid-state NMR determines weak couplings and long internuclear distances in peptides and proteins with selective isotopic labeling. This is a significant issue because most structurally interesting distances are long. After consideration of fractional labeling, natural abundance nuclei, and the population of molecules with random coil structures,

the *I*4 REDOR data were fit well to d_{CN} of 44.8 Hz and r_{CN} of 4.11 Å. The latter value agrees quantitatively with r_{CN} of an α helix which is the predominant conformation of the *I*4 peptide.

After consideration of fractional labeling and natural abundance nuclei, the GFF fpCTDQBU data were fit well to d_{CC} of 42.3 Hz and r_{CC} of 5.67 Å. These values are respectively ∼15% smaller and ∼5% larger than the crystallographic values. Possible contributions to this discrepancy include (1) vibrational averaging of d_{CC} through the large numbers of bonds between the two labeled nuclei and (2) inaccuracy in the D-GFF:unlabeled GFF ratio. Overall, the experiment was a robust measure of d_{CC} and r_{CC}.

Incorporation of finite π pulses in the fpCTDQBU experiment resulted in higher $\Delta S/S_0$ buildup rate and signal-to-noise. To our knowledge, previous application of fpRFDR sequences for distance determination has typically been done at high (≥20 kHz) MAS frequencies with the exception of work by Chan et al. on $^{31}P-^{31}P$ distances in phosphate compounds (*114*). The present work demonstrates application of fpRFDR at moderate spinning frequencies to measurement of structurally interesting and weak (<50 Hz) $^{13}C-^{13}C$ dipolar couplings. This is significant for membrane-associated peptides and proteins because it is often desirable to work at smaller protein:lipid ratio and therefore larger volume rotors with concomitant slower MAS frequencies. It was also found that constant-time was required to obtain interpretable RFDR data. Constant-time reduces signal intensity so reasonably high decoupling and judicious choice of the constant-time value were critical to obtain satisfactory data for the HFPtr sample. The fpCTDQBU sequence of the present study relies on the intensity difference of two spectra as a function of dephasing time while the related fpRFDR-CT method relies on the intensity of a single spectrum as a function of dephasing time (*51*, *65*). The fpRFDR-CT technique may therefore yield data with higher signal-to-noise.

ACKNOWLEDGMENT

We acknowledge the Michigan State mass spectrometry facility, the Michigan State Max T. Rogers NMR facility, and the Michigan Center for Biological Information for use of mass spectrometers, NMR spectrometers, and compute nodes, respectively. We acknowledge Dr. David L. DeWitt for use of his ultracentrifuge, Dr. Robert I. Cukier and Paul A. Reed for their assistance in installation of SIMPSON, and the SIMPSON/SIMMOL Discussion Forum for helpful discussion.

SUPPORTING INFORMATION AVAILABLE

Equations are derived for determination of $(\Delta S/S_0)^{cor}$ for REDOR and fpCTDQBU analyses. This material is available free of charge via the Internet at http://pubs.acs.org.

REFERENCES

1. Hernandez, L. D., Hoffman, L. R., Wolfsberg, T. G., and White, J. M. (1996) Virus-cell and cell-cell fusion, *Annu. Rev. Cell Dev. Biol. 12*, 627−661.
2. Eckert, D. M., and Kim, P. S. (2001) Mechanisms of viral membrane fusion and its inhibition, *Annu. Rev. Biochem. 70*, 777−810.
3. Colman, P. M., and Lawrence, M. C. (2003) The structural biology of type I viral membrane fusion, *Nat. Rev. Mol. Cell Biol. 4*, 309−319.
4. Freed, E. O., Myers, D. J., and Risser, R. (1990) Characterization of the fusion domain of the human immunodeficiency virus type 1 envelope glycoprotein gp41, *Proc. Natl. Acad. Sci. U.S.A. 87*, 4650−4654.
5. Pereira, F. B., Goni, F. M., Muga, A., and Nieva, J. L. (1997) Permeabilization and fusion of uncharged lipid vesicles induced by the HIV-1 fusion peptide adopting an extended conformation: dose and sequence effects, *Biophys. J. 73*, 1977−1986.
6. Mobley, P. W., Lee, H. F., Curtain, C. C., Kirkpatrick, A., Waring, A. J., and Gordon, L. M. (1995) The amino-terminal peptide of HIV-1 glycoprotein 41 fuses human erythrocytes, *Biochim. Biophys. Acta 1271*, 304−314.
7. Durell, S. R., Martin, I., Ruysschaert, J. M., Shai, Y., and Blumenthal, R. (1997) What studies of fusion peptides tell us about viral envelope glycoprotein-mediated membrane fusion, *Mol. Membr. Biol. 14*, 97−112.
8. Freed, E. O., Delwart, E. L., Buchschacher, G. L., Jr., and Panganiban, A. T. (1992) A mutation in the human immunodeficiency virus type 1 transmembrane glycoprotein gp41 dominantly interferes with fusion and infectivity, *Proc. Natl. Acad. Sci. U.S.A. 89*, 70−74.
9. Pereira, F. B., Goni, F. M., and Nieva, J. L. (1995) Liposome destabilization induced by the HIV-1 fusion peptide effect of a single amino acid substitution, *FEBS Lett. 362*, 243−246.
10. Kliger, Y., Aharoni, A., Rapaport, D., Jones, P., Blumenthal, R., and Shai, Y. (1997) Fusion peptides derived from the HIV type 1 glycoprotein 41 associate within phospholipid membranes and inhibit cell-cell Fusion. Structure- function study, *J. Biol. Chem. 272*, 13496−13505.
11. Suarez, T., Gallaher, W. R., Agirre, A., Goni, F. M., and Nieva, J. L. (2000) Membrane interface-interacting sequences within the ectodomain of the human immunodeficiency virus type 1 envelope glycoprotein: putative role during viral fusion, *J. Virol. 74*, 8038−8047.
12. Dimitrov, A. S., Rawat, S. S., Jiang, S., and Blumenthal, R. (2003) Role of the fusion peptide and membrane-proximal dornain in HIV-I envelope glycoprotein-mediated membrane fusion, *Biochemistry 42*, 14150−14158.
13. Shnaper, S., Sackett, K., Gallo, S. A., Blumenthal, R., and Shai, Y. (2004) The C- and the N-terminal regions of glycoprotein 41 ectodomain fuse membranes enriched and not enriched with cholesterol, respectively, *J. Biol. Chem. 279*, 18526−18534.
14. Pascual, R., Moreno, M. R., and Villalain, J. (2005) A peptide pertaining to the loop segment of human immunodeficiency virus gp41 binds and interacts with model biomembranes: Implications for the fusion mechanism, *J. Virol. 79*, 5142−5152.
15. Chan, D. C., Fass, D., Berger, J. M., and Kim, P. S. (1997) Core structure of gp41 from the HIV envelope glycoprotein, *Cell 89*, 263−273.
16. Tan, K., Liu, J., Wang, J., Shen, S., and Lu, M. (1997) Atomic structure of a thermostable subdomain of HIV-1 gp41, *Proc. Natl. Acad. Sci. U.S.A. 94*, 12303−12308.
17. Weissenhorn, W., Dessen, A., Harrison, S. C., Skehel, J. J., and Wiley: D. C. (1997) Atomic structure of the ectodomain from HIV-1 gp41, *Nature 387*, 426−430.
18. Caffrey, M., Cai, M., Kaufman, J., Stahl, S. J., Wingfield, P. T., Covell, D. G., Gronenborn, A. M., and Clore, G. M. (1998) Three-dimensional solution structure of the 44 kDa ectodomain of SIV gp41, *EMBO J. 17*, 4572−4584.
19. Yang, Z. N., Mueser, T. C., Kaufman, J., Stahl, S. J., Wingfield, P. T., and Hyde, C. C. (1999) The crystal structure of the SIV gp41 ectodomain at 1.47 A resolution, *J. Struct. Biol. 126*, 131−144.
20. Markosyan, R. M., Cohen, F. S., and Melikyan, G. B. (2003) HIV-1 envelope proteins complete their folding into six-helix bundles immediately after fusion pore formation, *Mol. Biol. Cell 14*, 926−938.
21. Dimitrov, A. S., Louis, J. M., Bewley, C. A., Clore, G. M., and Blumenthal, R. (2005) Conformational changes in HIV-1 gp41 in the course of HIV-1 envelope glycoprotein-mediated fusion and inactivation, *Biochemistry 44*, 12471−12479.
22. Rafalski, M., Lear, J. D., and DeGrado, W. F. (1990) Phospholipid interactions of synthetic peptides representing the N-terminus of HIV gp41, *Biochemistry 29*, 7917−7922.
23. Martin, I., Schaal, H., Scheid, A., and Ruysschaert, J. M. (1996) Lipid membrane fusion induced by the human immunodeficiency

virus type 1 gp41 N-terminal extremity is determined by its orientation in the lipid bilayer, *J. Virol. 70*, 298−304.
24. Curtain, C., Separovic, F., Nielsen, K., Craik, D., Zhong, Y., and Kirkpatrick, A. (1999) The interactions of the N-terminal fusogenic peptide of HIV-1 gp41 with neutral phospholipids, *Eur. Biophys. J. 28*, 427−436.
25. Yang, J., Gabrys, C. M., and Weliky, D. P. (2001) Solid-state nuclear magnetic resonance evidence for an extended beta strand conformation of the membrane-bound HIV-1 fusion peptide, *Biochemistry 40*, 8126−8137.
26. Gordon, L. M., Mobley, P. W., Pilpa, R., Sherman, M. A., and Waring, A. J. (2002) Conformational mapping of the N-terminal peptide of HIV-1 gp41 in membrane environments using ^{13}C-enhanced Fourier transform infrared spectroscopy, *Biochim. Biophys. Acta 1559*, 96−120.
27. Yang, J., Parkanzky, P. D., Bodner, M. L., Duskin, C. G., and Weliky, D. P. (2002) Application of REDOR subtraction for filtered MAS observation of labeled backbone carbons of membrane-bound fusion peptides, *J. Magn. Reson. 159*, 101−110.
28. Yang, R., Yang, J., and Weliky, D. P. (2003) Synthesis, enhanced fusogenicity, and solid state NMR measurements of cross-linked HIV-1 fusion peptides, *Biochemistry 42*, 3527−3535.
29. Bodner, M. L., Gabrys, C. M., Parkanzky, P. D., Yang, J., Duskin, C. A., and Weliky, D. P. (2004) Temperature dependence and resonance assignment of ^{13}C NMR spectra of selectively and uniformly labeled fusion peptides associated with membranes, *Magn. Reson. Chem. 42*, 187−194.
30. Castano, S., and Desbat, B. (2005) Structure and orientation study of fusion peptide FP23 of gp41 from HIV-1 alone or inserted into various lipid membrane models (mono-, bi- and multibi-layers) by FT-IR spectroscopies and Brewster angle microscopy, *Biochim. Biophys. Acta 1715*, 81−95.
31. Nieva, J. L., and Agirre, A. (2003) Are fusion peptides a good model to study viral cell fusion?, *Biochim. Biophys. Acta 1614*, 104−115.
32. Buzon, V., Padros, E., and Cladera, J. (2005) Interaction of fusion peptides from HIV gp41 with membranes: A time-resolved membrane binding, lipid mixing, and structural study, *Biochemistry 44*, 13354−13364.
33. Chang, D. K., Cheng, S. F., and Chien, W. J. (1997) The amino-terminal fusion domain peptide of human immunodeficiency virus type 1 gp41 inserts into the sodium dodecyl sulfate micelle primarily as a helix with a conserved glycine at the micelle-water interface, *J. Virol. 71*, 6593−6602.
34. Kamath, S., and Wong, T. C. (2002) Membrane structure of the human immunodeficiency virus gp41 fusion domain by molecular dynamics simulation, *Biophys. J. 83*, 135−143.
35. Maddox, M. W., and Longo, M. L. (2002) Conformational partitioning of the fusion peptide of HIV-1 gp41 and its structural analogs in bilayer membranes, *Biophys. J. 83*, 3088−3096.
36. Langham, A., and Kaznessis, Y. (2005) Simulation of the N-terminus of HIV-1 glycoprotein 41000 fusion peptide in micelles, *J. Pept. Sci. 11*, 215−224.
37. Morris, K. F., Gao, X. F., and Wong, T. C. (2004) The interactions of the HIV gp41 fusion peptides with zwitterionic membrane mimics determined by NMR spectroscopy, *Biochim. Biophys. Acta 1667*, 67−81.
38. Gordon, L. M., Mobley, P. W., Lee, W., Eskandari, S., Kaznessis, Y. N., Sherman, M. A., and Waring, A. J. (2004) Conformational mapping of the N-terminal peptide of HIV-1 gp41 in lipid detergent and aqueous environments using ^{13}C-enhanced Fourier transform infrared spectroscopy, *Protein Sci. 13*, 1012−1030.
39. Jaroniec, C. P., Kaufman, J. D., Stahl, S. J., Viard, M., Blumenthal, R., Wingfield, P. T., and Bax, A. (2005) Structure and dynamics of micelle-associated human immunodeficiency virus gp41 fusion domain, *Biochemistry 44*, 16167−16180.
40. Taylor, S. E., Desbat, B., Blaudez, D., Jacobi, S., Chi, L. F., Fuchs, H., and Schwarz, G. (2000) Structure of a fusion peptide analogue at the air-water interface, determined from surface activity, infrared spectroscopy and scanning force microscopy, *Biophys. Chem. 87*, 63−72.
41. Pritsker, M., Rucker, J., Hoffman, T. L., Doms, R. W., and Shai, Y. (1999) Effect of nonpolar substitutions of the conserved Phe11 in the fusion peptide of HIV-1 gp41 on its function, structure, and organization in membranes, *Biochemistry 38*, 11359−11371.
42. Gordon, L. M., Curtain, C. C., Zhong, Y. C., Kirkpatrick, A., Mobley, P. W., and Waring, A. J. (1992) The amino-terminal peptide of HIV-1 glycoprotein 41 interacts with human erythrocyte membranes: peptide conformation, orientation and aggregation, *Biochim. Biophys. Acta 1139*, 257−274.
43. Yang, J., and Weliky, D. P. (2003) Solid state nuclear magnetic resonance evidence for parallel and antiparallel strand arrangements in the membrane-associated HIV-1 fusion peptide, *Biochemistry 42*, 11879−11890.
44. Sackett, K., and Shai, Y. (2005) The HIV fusion peptide adopts intermolecular parallel b-sheet structure in membranes when stabilized by the adjacent N-terminal heptad repeat: A ^{13}C FTIR study, *J. Mol. Biol. 350*, 790−805.
45. Munoz-Barroso, I., Durell, S., Sakaguchi, K., Appella, E., and Blumenthal, R. (1998) Dilation of the human immunodeficiency virus-1 envelope glycoprotein fusion pore revealed by the inhibitory action of a synthetic peptide from gp41, *J. Cell Biol. 140*, 315−323.
46. Yang, R., Prorok, M., Castellino, F. J., and Weliky, D. P. (2004) A trimeric HIV-1 fusion peptide construct which does not self-associate in aqueous solution and which has 15-fold higher membrane fusion rate, *J. Am. Chem. Soc. 126*, 14722−14723.
47. Epand, R. F., Macosko, J. C., Russell, C. J., Shin, Y. K., and Epand, R. M. (1999) The ectodomain of HA2 of influenza virus promotes rapid pH dependent membrane fusion, *J. Mol. Biol. 286*, 489−503.
48. Lau, W. L., Ege, D. S., Lear, J. D., Hammer, D. A., and DeGrado, W. F. (2004) Oligomerization of fusogenic peptides promotes membrane fusion by enhancing membrane destabilization, *Biophys. J. 86*, 272−284.
49. Wexler-Cohen, Y., Sackett, K., and Shai, Y. (2005) The role of the N-terminal heptad repeat of HIV-1 in the actual lipid mixing step as revealed by its substitution with distant coiled coils, *Biochemistry 44*, 5853−5861.
50. Benzinger, T. L., Gregory, D. M., Burkoth, T. S., Miller-Auer, H., Lynn, D. G., Botto, R. E., and Meredith, S. C. (1998) Propagating structure of Alzheimer's β-amyloid(10-35) is parallel β-sheet with residues in exact register, *Proc. Natl. Acad. Sci. U.S.A. 95*, 13407−13412.
51. Balbach, J. J., Petkova, A. T., Oyler, N. A., Antzutkin, O. N., Gordon, D. J., Meredith, S. C., and Tycko, R. (2002) Supramolecular structure in full-length Alzheimer's β-amyloid fibrils: Evidence for a parallel β-sheet organization from solid-state nuclear magnetic resonance, *Biophys. J. 83*, 1205−1216.
52. Gullion, T., and Schaefer, J. (1989) Rotational-echo double-resonance NMR, *J. Magn. Reson. 81*, 196−200.
53. Anderson, R. C., Gullion, T., Joers, J. M., Shapiro, M., Villhauer, E. B., and Weber, H. P. (1995) Conformation of [1-^{13}C,^{15}N]acetyl-L-carnitine - rotational- echo, double-resonance nuclear-magnetic-resonance spectroscopy, *J. Am. Chem. Soc. 117*, 10546−10550.
54. Kimura, S., Naito, A., Saito, H., Ogawa, K., and Shoji, A. (2001) Characterization of α-helix structures in polypeptides, revealed by ^{13}C═O···H−^{15}N hydrogen bond lengths determined by ^{13}C REDOR NMR, *J. Mol. Struct. 562*, 197−203.
55. Murphy, O. J., 3rd, Kovacs, F. A., Sicard, E. L., and Thompson, L. K. (2001) Site-directed solid-state NMR measurement of a ligand-induced conformational change in the serine bacterial chemoreceptor, *Biochemistry 40*, 1358−1366.
56. Smith, S. O., Eilers, M., Song, D., Crocker, E., Ying, W. W., Groesbeek, M., Metz, G., Ziliox, M., and Aimoto, S. (2002) Implications of threonine hydrogen bonding in the glycophorin A transmembrane helix dimer, *Biophys. J. 82*, 2476−2486.
57. Nishimura, K., Kim, S. G., Zhang, L., and Cross, T. A. (2002) The closed state of a H^+ channel helical bundle combining precise orientational and distance restraints from solid state NMR, *Biochemistry 41*, 13170−13177.
58. Toke, O., Maloy, W. L., Kim, S. J., Blazyk, J., and Schaefer, J. (2004) Secondary structure and lipid contact of a peptide antibiotic in phospholipid Bilayers by REDOR, *Biophys. J. 87*, 662−674.
59. Mani, R., Tang, M., Wu, X., Buffy, J. J., Waring, A. J., Sherman, M. A., and Hong, M. (2006) Membrane-bound dimer structure of a beta-hairpin antimicrobial peptide from rotational-echo double-resonance solid-state NMR, *Biochemistry 45*, 8341−8349.
60. Long, J. R., Shaw, W. J., Stayton, P. S., and Drobny, G. P. (2001) Structure and dynamics of hydrated statherin on hydroxyapatite as determined by solid-state NMR, *Biochemistry 40*, 15451−15455.
61. Bennett, A. E., Ok, J. H., Griffin, R. G., and Vega, S. (1992) Chemical-shift correlation spectroscopy in rotating solids - radio frequency-driven dipolar recoupling and longitudinal exchange, *J. Chem. Phys. 96*, 8624−8627.

62. Gullion, T., and Vega, S. (1992) A simple magic angle spinning NMR experiment for the dephasing of rotational echoes of dipolar coupled homonuclear spin pairs, *Chem. Phys. Lett. 194*, 423−428.
63. Bennett, A. E., Rienstra, C. M., Griffiths, J. M., Zhen, W. G., Lansbury, P. T., and Griffin, R. G. (1998) Homonuclear radio frequency-driven recoupling in rotating solids, *J. Chem. Phys. 108*, 9463−9479.
64. Bennett, A. E., Weliky, D. P., and Tycko, R. (1998) Quantitative conformational measurements in solid state NMR by constant-time homonuclear dipolar recoupling, *J. Am. Chem. Soc. 120*, 4897−4898.
65. Ishii, Y. (2001) ^{13}C-^{13}C dipolar recoupling under very fast magic angle spinning in solid-state nuclear magnetic resonance: Applications to distance measurements, spectral assignments, and high-throughput secondary-structure determination, *J. Chem. Phys. 114*, 8473−8483.
66. Bak, M., Rasmussen, J. T., and Nielsen, N. C. (2000) SIMPSON: A general simulation program for solid-state NMR spectroscopy, *J. Magn. Reson. 147*, 296−330.
67. Chang, C. D., Waki, M., Ahmad, M., Meienhofer, J., Lundell, E. O., and Haug, J. D. (1980) Preparation and properties of N-α-9-fluorenylmethyloxycarbonylamino acids bearing tert-butyl side chain protection, *Int. J. Pept. Protein Res. 15*, 59−66.
68. Lapatsanis, L., Milias, G., Froussios, K., and Kolovos, M. (1983) Synthesis of N-2,2,2-(trichloroethoxycarbonyl)-L-amino acids and N-(9-fluorenylmethoxycarbonyl)-L-amino acids involving succinimidoxy anion as a leaving group in amino-acid protection, *Synthesis 8*, 671−673.
69. Williamson, K. L. (1994) *Macroscale and Microscale Organic Experiments*, 2nd ed., Heath and Company, Lexington, MA, Toronto.
70. Waskowska, A., Lukaszewicz, K., Kuzmina, L. G., Strutshkov, Y. T. (1975) The Crystal Structure of N-acetyl-L-leucine, *Bull. Pol. Acad. Sci. Ser. Sci. Chim. 23*, 149−153.
71. Precigoux, G., Cotrait, M., and Geoffre, S. (1986) Structure of glycyl-L-phenylalanyl-L-phenylalanine hemihydrate, *Acta Crystallogr., Sect. C 42*, 315−317.
72. Long, H. W., and Tycko, R. (1998) Biopolymer conformational distributions from solid-state NMR: α-helix and 3_{10}-helix contents of a helical peptide, *J. Am. Chem. Soc. 120*, 7039−7048.
73. Macosko, J. C., Kim, C. H., and Shin, Y. K. (1997) The membrane topology of the fusion peptide region of influenza hemagglutinin determined by spin-labeling EPR, *J. Mol. Biol. 267*, 1139−1148.
74. Han, X., Bushweller, J. H., Cafiso, D. S., and Tamm, L. K. (2001) Membrane structure and fusion-triggering conformational change of the fusion domain from influenza hemagglutinin, *Nat. Struct. Biol. 8*, 715−720.
75. Afonin, S., Dur, U. H. N., Glaser, R. W., and Ulrich, A. S. (2004) 'Boomerang'-like insertion of a fusogenic peptide in a lipid membrane revealed by solid-state ^{19}F NMR, *Magn. Reson. Chem. 42*, 195−203.
76. Wasniewski, C. M., Parkanzky, P. D., Bodner, M. L., and Weliky, D. P. (2004) Solid-state nuclear magnetic resonance studies of HIV and influenza fusion peptide orientations in membrane bilayers using stacked glass plate samples, *Chem. Phys. Lipids 132*, 89−100.
77. Aloia, R. C., Tian, H., and Jensen, F. C. (1993) Lipid composition and fluidity of the human immunodeficiency virus envelope and host cell plasma membranes, *Proc. Natl. Acad. Sci. U.S.A. 90*, 5181−5185.
78. Brugger, B., Glass, B., Haberkant, P., Leibrecht, I., Wieland, F. T., and Krasslich, H. G. (2006) The HIV lipidome: A raft with an unusual composition, *Proc. Natl. Acad. Sci. U.S.A. 103*, 2641−2646.
79. Hope, M. J., Bally, M. B., Webb, G., and Cullis, P. R. (1985) Production of large unilamellar vesicles by a rapid extrusion procedure - characterization of size distribution, trapped volume and ability to maintain a membrane-potential, *Biochim. Biophys. Acta 812*, 55−65.
80. Morcombe, C. R., and Zilm, K. W. (2003) Chemical shift referencing in MAS solid state NMR, *J. Magn. Reson. 162*, 479−486.
81. Zhang, H. Y., Neal, S., and Wishart, D. S. (2003) RefDB: A database of uniformly referenced protein chemical shifts, *J. Biomol. NMR 25*, 173−195.
82. Bennett, A. E., Rienstra, C. M., Auger, M., Lakshmi, K. V., and Griffin, R. G. (1995) Heteronuclear decoupling in rotating solids, *J. Chem. Phys. 103*, 6951−6958.
83. Gullion, T. (1998) Introduction to rotational-echo, double-resonance NMR, *Concepts Magn. Reson. 10*, 277−289.
84. McDowell, L. M., Holl, S. M., Qian, S. J., Li, E., and Schaefer, J. (1993) Inter-tryptophan distances in rat cellular retinol-binding Protein II by solid-state NMR, *Biochemistry 32*, 4560−4563.
85. Balazs, Y. S., and Thompson, L. K. (1999) Practical methods for solid-state NMR distance measurements on large biomolecules: Constant-time rotational resonance, *J. Magn. Reson. 139*, 371−376.
86. Bevington, P. R., and Robinson, D. K. (1992) *Data Reduction and Error Analysis for the Physical Sciences*, 2nd ed., McGraw-Hill, Boston.
87. Oas, T. G., Hartzell, C. J., McMahon, T. J., Drobny, G. P., and Dahlquist, F. W. (1987) The carbonyl ^{13}C chemical shift tensors of 5 peptides determined from ^{15}N dipole-coupled chemical shift powder patterns, *J. Am. Chem. Soc. 109*, 5956−5962.
88. Herzfeld, J., and Berger, A. E. (1980) Sideband intensities in NMR spectra of samples spinning at the magic angle, *J. Chem. Phys. 73*, 6021−6030.
89. Naito, A., Ganapathy, S., Akasaka, K., and McDowell, C. A. (1981) Chemical shielding tensor and ^{13}C-^{14}N dipolar splitting in single crystals of L-alanine, *J. Chem. Phys. 74*, 3190−3197.
90. Facelli, J. C., Gu, Z. T., and McDermott, A. (1995) Carbon-13 chemical-shift tensors of carboxylic-acids: GIAO calculations in acetic-acid + methylamine dimer, *Mol. Phys. 86*, 865−872.
91. Longhi, S., Czjzek, M., Lamzin, V., Nicolas, A., and Cambillau, C. (1997) Atomic resolution (1.0 Å) crystal structure of Fusarium solani cutinase: stereochemical analysis, *J. Mol. Biol. 268*, 779−799.
92. Basak, A., Bateman, O., Slingsby, C., Pande, A., Asherie, N., Ogun, O., Benedek, G. B., and Pande, J. (2003) High-resolution X-ray crystal structures of human gD crystallin (1.25 Å) and the R58H mutant (1.15 Å) associated with aculeiform cataract, *J. Mol. Biol. 328*, 1137−1147.
93. Schmidt-Rohr, K., and Spiess, H. W. (1994) *Multidimensional Solid-State NMR and Polymers*, 2nd ed., Academic Press, San Diego.
94. Press: W. H., Teukolsky, S. A., Vetterling, W. T., and Flannery, B. P. (1996) *Numerical Recipes in FORTRAN 77: The Art of Scientific Computing*, Vol. Fortran Numerical Recipes, 2nd ed., Cambridge, New York.
95. Kricheldorf, H. R., and Muller, D. (1983) Secondary structure of peptides. 3. ^{13}C NMR cross polarization/magic angle spinning spectroscopic characterization of solid polypeptides, *Macromolecules 16*, 615−623.
96. Saito, H. (1986) Conformation-dependent ^{13}C chemical shifts - a new means of conformational characterization as obtained by high-resolution solid-state ^{13}C NMR, *Magn. Reson. Chem. 24*, 835−852.
97. Bodner, M. L. (2006) Solid state nuclear magnetic resonance of the HIV-1 and influenza fusion peptides associated with membranes, Ph.D. Thesis, Michigan State University, East Lansing.
98. Yang, J., Prorok, M., Castellino, F. J., and Weliky, D. P. (2004) Oligomeric beta structure of the membrane-bound HIV-1 fusion peptide formed from soluble monomers, *Biophys. J. 87*, 1951−1963.
99. Bloom, M., Evans, E., and Mouritsen, O. G. (1991) Physical properties of the fluid lipid-bilayer component of cell membranes: a perspective, *Q. Rev. Biophys. 24*, 293−397.
100. Smaby, J. M., Momsen, M. M., Brockman, H. L., and Brown, R. E. (1997) Phosphatidylcholine acyl unsaturation modulates the decrease in interfacial elasticity induced by cholesterol, *Biophys. J. 73*, 1492−1505.
101. Li, X. M., Momsen, M. M., Smaby, J. M., Brockman, H. L., and Brown, R. E. (2001) Cholesterol decreases the interfacial elasticity and detergent solubility of sphingomyelins, *Biochemistry 40*, 5954−5963.
102. Silvius, J. R. (2003) Role of cholesterol in lipid raft formation: lessons from lipid model systems, *Biochim. Biophys. Acta 1610*, 174−183.
103. Binder, W. H., Barragan, V., and Menger, F. M. (2003) Domains and rafts in lipid membranes, *Angew. Chem., Int. Ed. 42*, 5802−5827.
104. Simons, K., and Vaz, W. L. C. (2004) Model systems, lipid rafts, and cell membranes, *Annu. Rev. Biophys. Biomol. Struct. 33*, 269−295.
105. McMullen, T. P. W., Lewis, R., and McElhaney, R. N. (2004) Cholesterol-phospholipid interactions, the liquid-ordered phase and

lipid rafts in model and biological membranes, *Curr. Opin. Colloid Interface Sci. 8*, 459−468.
106. Saez-Cirion, A., and Nieva, J. L. (2002) Conformational transitions of membrane-bound HIV-1 fusion peptide, *Biochim. Biophys. Acta 1564*, 57−65.
107. Afonin, S., Glaser, R. W., Berditchevskaia, M., Wadhwani, P., Guhrs, K. H., Mollmann, U., Perner, A., and Ulrich, A. S. (2003) 4-fluorophenylglycine as a label for ^{19}F NMR structure analysis of membrane-associated peptides, *ChemBioChem 4*, 1151−1163.
108. Hofmann, M. W., Weise, K., Ollesch, J., Agrawal, P., Stalz, H., Stelzer, W., Hulsbergen, F., de Groot, H., Gerwert, K., Reed, J., and Langosch, D. (2004) De novo design of conformationally flexible transmembrane peptides driving membrane fusion, *Proc. Natl. Acad. Sci. U.S.A. 101*, 14776−14781.
109. Parkanzky, P. D. (2006) Solid state nuclear magnetic resonance studies of the influenza fusion peptide associated with membrane bilayers, Ph.D. Thesis, Michigan State University, East Lansing.
110. Haque, M. E., Koppaka, V., Axelsen, P. H., and Lentz, B. R. (2005) Properties and structures of the influenza and HIV fusion peptides on lipid membranes: Implications for a role in fusion, *Biophys. J. 89*, 3183−3194.
111. Ono, A., and Freed, E. O. (2005) Role of lipid rafts in virus replication, in *Virus Structure And Assembly* (Roy, P., Ed.) pp 311−358, Elsevier Academic Press, San Diego.
112. Nieva, J. L., Nir, S., Muga, A., Goni, F. M., and Wilschut, J. (1994) Interaction of the HIV-1 fusion peptide with phospholipid vesicles: different structural requirements for fusion and leakage, *Biochemistry 33*, 3201−3209.
113. Gordon, D. J., Balbach, J. J., Tycko, R., and Meredith, S. C. (2004) Increasing the amphiphilicity of an amyloidogenic peptide changes the beta-sheet structure in the fibrils from antiparallel to parallel, *Biophys. J. 86*, 428−434.
114. Tseng, Y. H., Mou, Y., Mou, C. Y., and Chan, J. C. C. (2005) Double-quantum NMR spectroscopy based on finite pulse RFDR, *Solid State Nucl. Magn. Reson. 27*, 266−270.

BI0615902